

TOWARD UNIFIED CORRECTION OF REGIONAL PHASES FOR AMPLITUDE AND TRAVEL TIME EFFECTS OF HETEROGENEOUS STRUCTURE Annual Report

T. Lay, et al.

**University of California Santa Cruz
Department of Earth and Planetary Sciences
1156 High Street
Santa Cruz, California 95064**

01 November 2014

Technical Report

APPROVED FOR PUBLIC RELEASE; DISTRIBUTION IS UNLIMITED.



**AIR FORCE RESEARCH LABORATORY
Space Vehicles Directorate
3550 Aberdeen Ave SE
AIR FORCE MATERIEL COMMAND
KIRTLAND AIR FORCE BASE, NM 87117-5776**

DTIC COPY

NOTICE AND SIGNATURE PAGE

Using Government drawings, specifications, or other data included in this document for any purpose other than Government procurement does not in any way obligate the U.S. Government. The fact that the Government formulated or supplied the drawings, specifications, or other data does not license the holder or any other person or corporation; or convey any rights or permission to manufacture, use, or sell any patented invention that may relate to them.

This report was cleared for public release by the 377 ABW Public Affairs Office and is available to the general public, including foreign nationals. Copies may be obtained from the Defense Technical Information Center (DTIC) (<http://www.dtic.mil>).

AFRL-RV-PS-TP-2015-0009 HAS BEEN REVIEWED AND IS APPROVED FOR PUBLICATION IN ACCORDANCE WITH ASSIGNED DISTRIBUTION STATEMENT.

//SIGNED//

Dr. Robert Raistrick
Project Manager, AFRL/RVBYE

//SIGNED//

Glenn M. Vaughan, Colonel, USAF
Chief, Battlespace Environment Division

This report is published in the interest of scientific and technical information exchange, and its publication does not constitute the Government's approval or disapproval of its ideas or findings.

REPORT DOCUMENTATION PAGE				<i>Form Approved</i> OMB No. 0704-0188	
Public reporting burden for this collection of information is estimated to average 1 hour per response, including the time for reviewing instructions, searching existing data sources, gathering and maintaining the data needed, and completing and reviewing this collection of information. Send comments regarding this burden estimate or any other aspect of this collection of information, including suggestions for reducing this burden to Department of Defense, Washington Headquarters Services, Directorate for Information Operations and Reports (0704-0188), 1215 Jefferson Davis Highway, Suite 1204, Arlington, VA 22202-4302. Respondents should be aware that notwithstanding any other provision of law, no person shall be subject to any penalty for failing to comply with a collection of information if it does not display a currently valid OMB control number. PLEASE DO NOT RETURN YOUR FORM TO THE ABOVE ADDRESS.					
1. REPORT DATE (DD-MM-YYYY) 01-11-2014		2. REPORT TYPE Technical Report		3. DATES COVERED (From - To) 03 Aug 2013 – 04 Aug 2014	
4. TITLE AND SUBTITLE TOWARD UNIFIED CORRECTION OF REGIONAL PHASES FOR AMPLITUDE AND TRAVEL TIME EFFECTS OF HETEROGENEOUS STRUCTURE Annual Report				5a. CONTRACT NUMBER FA9453-12-C-0234	
				5b. GRANT NUMBER	
				5c. PROGRAM ELEMENT NUMBER 62601F	
6. AUTHOR(S) T. Lay, X.-B. Xie, and X. Yang				5d. PROJECT NUMBER 1010	
				5e. TASK NUMBER PPM00014494	
				5f. WORK UNIT NUMBER EF007787	
7. PERFORMING ORGANIZATION NAME(S) AND ADDRESS(ES) University of California Santa Cruz Department of Earth and Planetary Sciences 1156 High Street Santa Cruz, CA 95064				8. PERFORMING ORGANIZATION REPORT NUMBER	
9. SPONSORING / MONITORING AGENCY NAME(S) AND ADDRESS(ES) Air Force Research Laboratory Space Vehicles Directorate 3550 Aberdeen Avenue SE Kirtland AFB, NM 87117-5776				10. SPONSOR/MONITOR'S ACRONYM(S) AFRL/RVBYE	
				11. SPONSOR/MONITOR'S REPORT NUMBER(S) AFRL-RV-PS-TP-2015-0009	
12. DISTRIBUTION / AVAILABILITY STATEMENT Approved for public release; distribution is unlimited. (OPS-15-7321 dtd 18 Nov 2015)					
13. SUPPLEMENTARY NOTES					
14. ABSTRACT Regional seismic models used for travel times in event location procedures are explored for use in amplitude corrections for geometric spreading. The goal is to evaluate whether it is viable to have self-consistent representations of the travel time and spreading models as the structural representations have improved.					
15. SUBJECT TERMS Explosion modeling, Geometric spreading of Pn, Regional travel time models					
16. SECURITY CLASSIFICATION OF:			17. LIMITATION OF ABSTRACT Unlimited	18. NUMBER OF PAGES 40	19a. NAME OF RESPONSIBLE PERSON Dr. Robert Raistrick
a. REPORT Unclassified	b. ABSTRACT Unclassified	c. THIS PAGE Unclassified			19b. TELEPHONE NUMBER (include area code)

This page is intentionally left blank.

Table of Contents

1. SUMMARY	1
2. INTRODUCTION	1
3. BACKGROUND AND TECHNICAL APPROACH	2
4. RESULTS AND DISCUSSION	15
5. PRELIMINARY FINDINGS	29
REFERENCES	30

List of Figures

1. Base Earth Model used for Pn and Sn simulations and the development of new Pn and Sn geometric-spreading models	3
2. 10-Hz synthetic Pn amplitude decay in the spherical Base Earth Model with constant mantle velocities	4
3. Synthetic Pn amplitudes as a function of epicentral distance and frequency	4
4. Pn amplitude versus distance curves similar to Figure 3, but for the Base Earth Model (red curves, for no physical gradient in the lid) and for two models with mild positive gradients in the mantle lid.....	6
5. Visualizations of 2D velocity model with (top) 0.5% (rms) P -velocity heterogeneity in the upper one hundred kilometers of the mantle lid, and (bottom) exponential 3% (rms) roughness of the Moho with 40 km scale averaging length.....	7
6. Ensemble-averaged Pn amplitudes as a function of distance for all configurations of random volumetric mantle heterogeneity simulated. Pn amplitude for the BEM (diamonds) are compared to models with 0.5% RMS (squares), 1.0% RMS (triangles), and 2% RMS (X's) V_p fluctuation for horizontal (A_x) and vertical (A_y) averaging lengths of (a) $A_x = 10$ km, $A_y = 10$ km (isotropic); (b) $A_x = 20$ km, $A_y = 10$ km; (c) $A_x = 20$ km, $A_y = 6$ km; and (d) $A_x = 40$ km, $A_y = 3$ km	8
7. Ensemble-averaged Pn amplitudes plotted as a function of distance for all configurations of random Moho topography heterogeneity, grouped by percent RMS depth fluctuation	9
8. 1-Hz Pn amplitudes after source and geometric-spreading correction using the model developed by Yang et al. (2007)	10
9. 1-Hz Pn amplitudes after source and geometric-spreading correction using the new model developed by Yang (2011).....	11
10. Comparison of 1-Hz Pn amplitude decay with decays predicted by a power-law spreading model and by the new spreading model of Yang <i>et al.</i> (2007)	12
11. Comparison of average Q estimates from Pn amplitudes corrected for source and geometric-spreading effects using different spreading models. Q estimates at 1, 4 and 8 Hz are compared	13
12. Global model parameterization. (a) An example tessellation with approximately 5° grid spacing. (b) An example velocity vs. depth profile as defined at each node.....	13

13. Comparison of starting and RSTT models. (a) Velocity below the Moho for starting model and (b) RSTT model. (c) Mantle gradient (km/sec/km) for starting model and (d) RSTT model.....	14
14. Snapshots of wavefields computed for 1D structures (constant lid gradient is w/o EFT) using the enhanced 2D finite-difference code implementation	15
15. Vertical component synthetic seismograms computed by the 2D finite-difference code plotted with a reduction velocity of 8.1 km/s, which is the constant lid velocity in the basic Earth model (BEM)	16
16. Reference velocity models considered as 1D structures or end-members of 2D structures with laterally varying mantle lid gradients for broadband Pn waveform computations up to 10 Hz at 1000 km distance	17
17. Arrival time picks from profiles of synthetics in Figure 15 displaying the weak curvature introduced by linear mantle lid gradients	18
18. Pn amplitude decay as a function of narrowband frequency versus distance for models in Figure 16	19
19. Pn amplitude decay as a function of narrowband frequency versus distance for models in Figure 16	19
20. 2D velocity models with laterally varying mantle lid velocity gradients that vary beneath the source and receiver locations.....	20
21. Pn amplitude versus distance for 1D (Figure 16) and 2D models (Figure 20) for varying bandpass center frequencies.	21
22. Pn amplitude versus distance for 1D (Figure 16) and 2D models (Figure 20) for a 3.75 Hz center frequency of a narrow bandpass	22
23. RSTT model lid velocity gradients (top) and average Moho P velocity (bottom) with a superimposed grid developed to define provinces of similar parameters	23
24. LANL Eurasian Pn data base coverage showing Pn paths sampling the RSTT-based regionalization.....	24
25. Regional numbering scheme for the RSTT-based subdivision.....	24
26a. Pn amplitudes versus distance for Region 4 with corrections using a power-law (top row), RSTT-based synthetic computations (middle row) or empirical region-specific corrections following the procedure of Yang (2011) (bottom row) for passband center frequencies of 1.06 Hz (left) and 4.24 Hz (right)	25

26b. Pn amplitudes versus distance for Region 4 (map inset) with corrections using a power-law (top row), RSTT-based synthetic computations (middle row) or empirical region-specific corrections following the procedure of Yang (2011) (bottom row) for passband center frequency of 8.94 Hz (right)	26
27a. Pn amplitudes versus distance for Region 13 with corrections using a power-law (top row), RSTT-based synthetic computations (middle row) or empirical region-specific corrections following the procedure of Yang (2011) (bottom row) for passband center frequencies of 1.06 Hz (left) and 4.24 Hz (right)	27
27b. Pn amplitudes versus distance for Region 13 (map inset) with corrections using a power-law (top row), RSTT-based synthetic computations (middle row) or empirical region-specific corrections following the procedure of Yang (2011) (bottom row) for passband center frequency of 8.94 Hz (right)	28

1. SUMMARY

Regional seismic phases (e.g., Pn , Sn , Pg , Lg) play a very important role in global monitoring of low yield underground nuclear tests. Given a typical paucity of teleseismic observations for a small event, regional phase arrival times can be critical for locating the source. Numerous empirical observations have also shown that regional phases hold the keys to small event magnitude and yield estimation and to discrimination between small explosions and earthquakes (e.g., Taylor et al., 1989; Kim et al., 1997; Walter et al., 1995; Fisk et al., 1996, 2005; Taylor, 1996; Taylor and Hartse, 1997; Hartse et al., 1997; Patton, 2001; Xie, 2002; Richards and Kim 2007; Zhao et al., 2008). Use of travel times and amplitudes of regional phases for location, discrimination and yield estimation procedures requires that the regional velocity and attenuation structures be sufficiently well approximated (e.g., Myers et al., 2010). As a result there have been extensive efforts to determine regional crustal and upper mantle velocity models and tomographic models for attenuation of regional phases. These efforts commonly proceed independently, with geometric spreading models being used for simple or generic structures even while detailed regional velocity models are determined for travel times. This situation is evolving, with an increasing emphasis on model-based procedures rather than on empirical data trends entering into operational systems, and this presents both challenges and opportunities for developing self-consistent model-based procedures. The guiding theme of this project is working toward unified, self-consistent correction of regional phases for amplitude and travel time effects of heterogeneous Earth structure. Our focus is on two of the critical regional phases, Pn and Sn , which traverse the uppermost mantle, and commonly are assumed to have very simple wave behavior controlling their amplitudes and travel times. In fact, both phases have complex sensitivity to Earth structure that is not well represented by standard processing assumptions (particularly when determining attenuation models needed for the model-based procedures), motivating use of regionally appropriate velocity structures, just as are motivated for precise event location. Striving toward self-consistency of regional structures used for travel time and amplitude analysis is a logical step as model-based approaches are adopted in the operational environment.

2. INTRODUCTION

This project builds on a prior collaboration in which we developed geometric spreading corrections for regional phases Pn and Sn for simple reference velocity models and applied these to develop frequency-dependent Pn attenuation models for Eurasia. We confirmed that these seismic phases have acute sensitivity to structure, with frequency-dependent geometric spreading behavior for even the simplest spherical structures. The sensitivity to mantle-lid velocity gradient is non-linear and pronounced, but can be characterized well by numerical modeling for specific structures. Current procedures tend to ignore the complex geometric spreading of these phases and thus likely project artificial frequency dependence into attenuation models for the mantle lid. Practical determination of precise regional mantle-lid velocity gradients is challenging, but possible if curvature of Pn and Sn travel time branches is constrained in a local region.

This is exactly what is being performed in RSTT (regional seismic travel time) approaches, although data scatter and trade-off with variable crustal legs certainly reduces confidence in inferred mantle-lid radial velocity gradients. We are exploring the predictions of RSTT and similar models for amplitude effects, considering both the implications for associated frequency-dependent attenuation models and the prospects of jointly using amplitude and travel time information to better constrain the regional velocity and attenuation structures. Eurasian datasets of regional Pn and Sn phases will be utilized, and our previous work on determining frequency-dependent geometric spreading as a function of 1D velocity model variations will be expanded to provide corrections for laterally varying regional composites. We will also apply a 3D modeling approach (involving acoustic 1-way propagators) to evaluate effects of laterally varying structure on the geometric spreading predictions, extending our current (up to 10 Hz) 2D finite-difference modeling efforts to more realistic media. Waveform attributes, such as frequency-dependent amplitude ratios of first Pn arrival to early Pn coda, that may help to constrain the actual mantle-lid velocity gradient will be evaluated using the synthetics and data. The ultimate goal is to work toward procedures for determining regional attenuation and velocity models that are useful for self-consistently correcting both travel-time and amplitude measurements for improved event location, event identification and magnitude/yield determination.

3. BACKGROUND AND TECHNICAL APPROACH

Pn and Sn geometric spreading

Accurately accounting for geometric spreading is critical for the development of meaningful regional-phase attenuation models. This is particularly true for Pn and Sn waves because the nature of their wave propagation renders them acutely sensitive to uppermost mantle velocity structure and Earth's sphericity. Even simple one-dimensional (1D) velocity models can produce geometric spreading of Pn and Sn that is strongly dependent on frequency (e.g., Sereno and Given, 1990; Yang et al., 2007; Avants et al., 2011). If frequency dependence of the geometric spreading is neglected, any inferred attenuation model based on using that geometric spreading will acquire incorrect frequency dependence.

In our previous modeling efforts, we generated synthetic seismograms for a 1D, spherical Earth model (Yang et al., 2007; Avants et al., 2011) to simulate Pn and Sn geometric spreading in such a structure. We used the same generic spherical Earth model considered by Sereno and Given (1990) as the Base Earth Model for our simulations (Figure 1) and developed new Pn and Sn geometric-spreading models using the synthetics from the simulation.

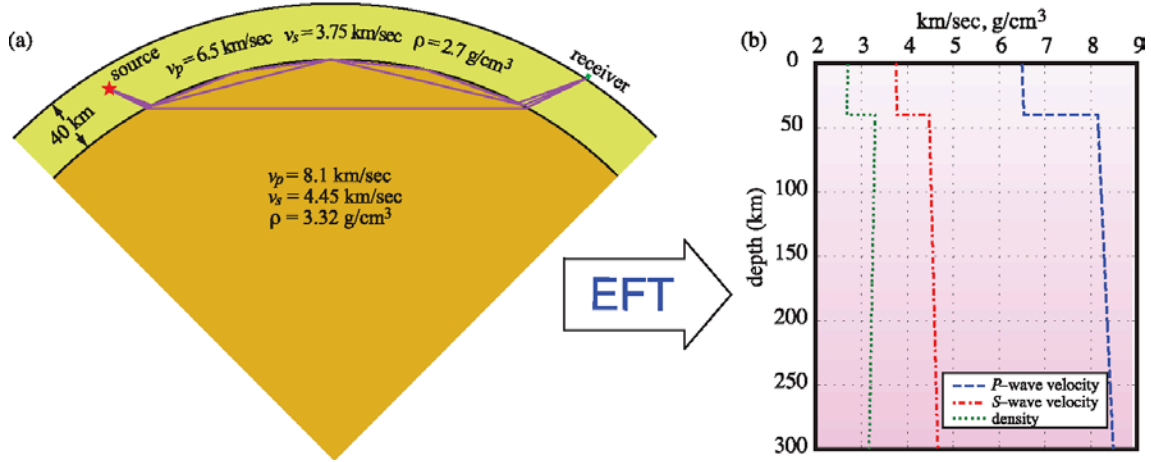


Figure 1. Base Earth Model used for P_n and S_n simulations and the development of new P_n and S_n geometric-spreading models. *Quality factor Q is infinite throughout the model. Earth flattening transform yields the 1D models on the right, which have mild positive velocity gradients even though the mantle lid has constant velocity in the spherical structure.*

We computed synthetic seismograms using the source parameterizations and procedures described in detail by Yang et al. (2007) and extracted the P_n and S_n portions of the synthetic seismograms using fixed-velocity windows. We measured P_n and S_n amplitudes from the spectra calculated using the P_n and S_n synthetic seismograms. The 10-Hz P_n amplitude decay in the spherical Base Earth Model is shown in Figure 2. Also plotted in the figure is the amplitude decay of a conical head wave in a plane one-layer-over-half-space model (Aki and Richards, 2002; Eq. 6.26) and the amplitude decay of infinite-frequency direct wave in a spherical Earth model from ray tracing. At distances close to the critical distance, P_n geometric spreading behaves like that of a conical head wave. As distance increases, P_n spreading starts to deviate from that of the head wave and at about 5° , P_n amplitudes begin to increase. In the range between the critical distance and about 10° , P_n evolves from a wave similar to a conical head wave to the interference head wave, which is a superposition of multiple waves reflected from the Moho. At teleseismic distances, the direct-wave spreading approaches that of the infinite-frequency diving P wave from ray tracing.

P_n geometric spreading in a spherical Earth model is not only different from that of a head wave as is shown in Figure 2, but also frequency dependent. Figure 3 shows the P_n amplitude-variation surface as a function of distance and frequency for the simple Base Earth Model. The strong frequency dependence of P_n amplitudes is apparent. Amplitudes at higher frequencies are affected more by sphericity than are lower-frequency amplitudes.

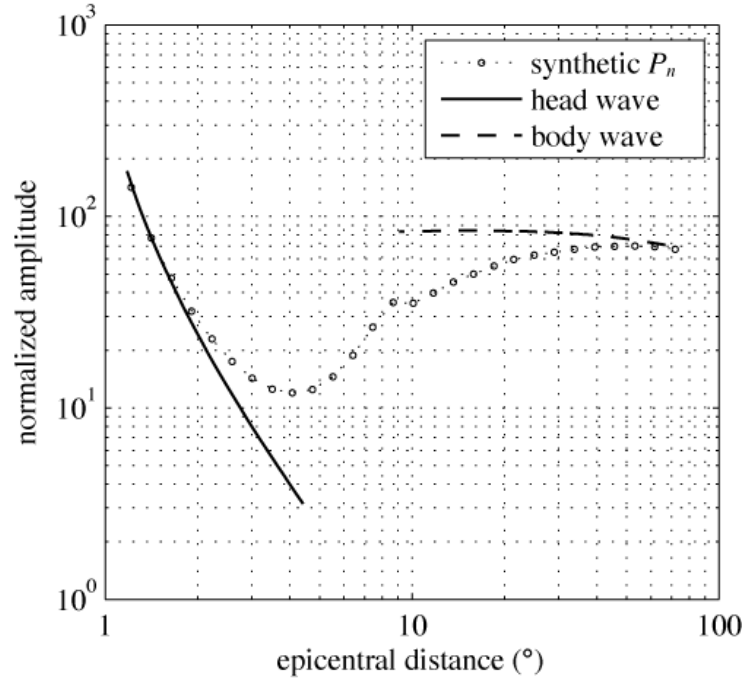


Figure 2. 10-Hz synthetic P_n amplitude decay in the spherical Base Earth Model with constant mantle velocities. *The solid line depicts the theoretical amplitude decay of a conical head wave in a plane one-layer-over-half-space Earth model. The dashed line is the amplitude decay of infinite-frequency direct wave in a spherical homogeneous Earth model from ray-tracing calculations. From Yang et al. (2007).*

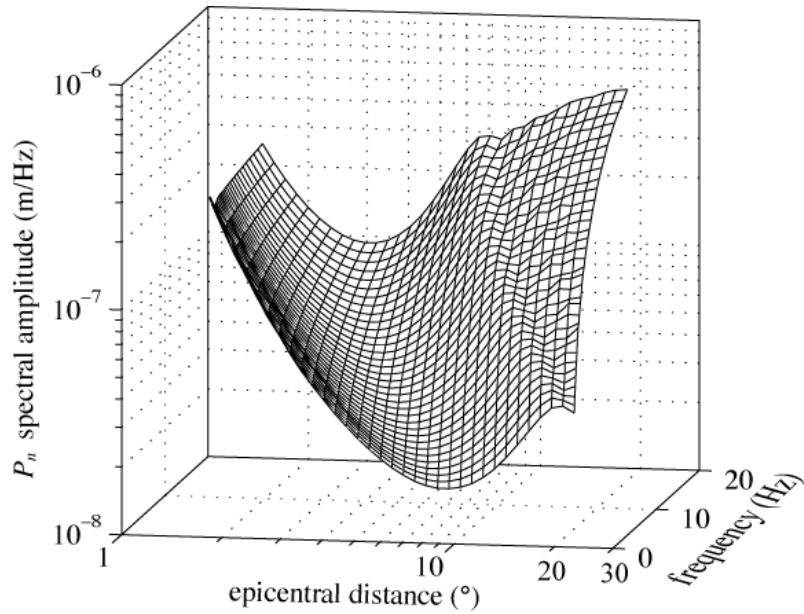


Figure 3. Synthetic P_n amplitudes as a function of epicentral distance and frequency. *From Yang et al. (2007).*

Yang et al. (2007) presented a parameterized description of *Pn* geometric spreading for this simple reference model. The amplitude spectrum of *Pn* can be parameterized as

$$A(r, \theta, f) = K(f) M_0 R(\theta) G(r, f) \exp\left(-\frac{\pi f}{Q(f) v} r\right) S(f) \quad (1)$$

with the new geometric-spreading model expressed as

$$G(r, f) = \frac{10^{n_3(f)}}{r_0} \left(\frac{r_0}{r}\right)^{n_1(f) \log\left(\frac{r_0}{r}\right) + n_2(f)} \quad (r_0 = 1 \text{ km}) \quad (2)$$

and

$$n_i(f) = n_{i1} \left[\log\left(\frac{f}{f_0}\right) \right]^2 + n_{i2} \log\left(\frac{f}{f_0}\right) + n_{i3} \quad (i = 1, 2, 3; f_0 = 1 \text{ Hz}). \quad (3)$$

In Equation 1, K is a frequency-dependent scaling factor; M_0 is source moment; R is source radiation pattern; Q is *Pn* quality factor; v is *Pn* velocity; S is receiver site response; r is epicentral distance; θ is azimuth angle and f is frequency. r_0 and f_0 are included in Equations (2) and (3) in order for the new model to have the same dimension as standard power-law models. Yang et al. (2007) derived the coefficients n_{ij} by fitting Equations (2) and (3) to the synthetic data. As a result, the new spreading models better represent *Pn* and *Sn* geometric spreading in a more realistic Earth. The main differences between the new geometric-spreading model and the standard frequency-independent power-law model are the addition of the first term in the exponent and the frequency dependence of parameters n_i .

***Pn* Spreading Sensitivity to Mantle Velocity Gradients**

The velocity structure of the mantle lid is seldom well constrained. The most direct constraint is provided by the shape of the *Pn* travel time curve as a function of distance over a wide-enough distance range for reliable measurement, and even when there is apparent travel time branch curvature, it is difficult to distinguish between a smooth gradient with depth versus constant velocity layering with small step increases. Receiver function methods and surface wave dispersion inversions sometimes indicate gradients in the lid structure, but resolution tends to be poor, especially for *P*-velocity. As a result, reference velocity structures often assume constant or near-constant velocity in the mantle lid by default, so the Base Earth Model is not a bad starting point in many cases. However, there are regions where the lid velocity appears to increase or decrease with depth. The effects of positive *P*-velocity gradients in the mantle lid on the frequency-dependent spreading of *Pn* are illustrated in Figure 4. The basic shape of the spreading behavior is preserved, but the distance-behavior shifts systematically to shorter distances, with overall higher *Pn* amplitudes as the gradient increases. It is possible to determine appropriate coefficients for a spreading representation like Equation (2) for any specific gradient, but this is only warranted if there are a priori constraints on the specific model in the region for which the spreading is to be utilized.

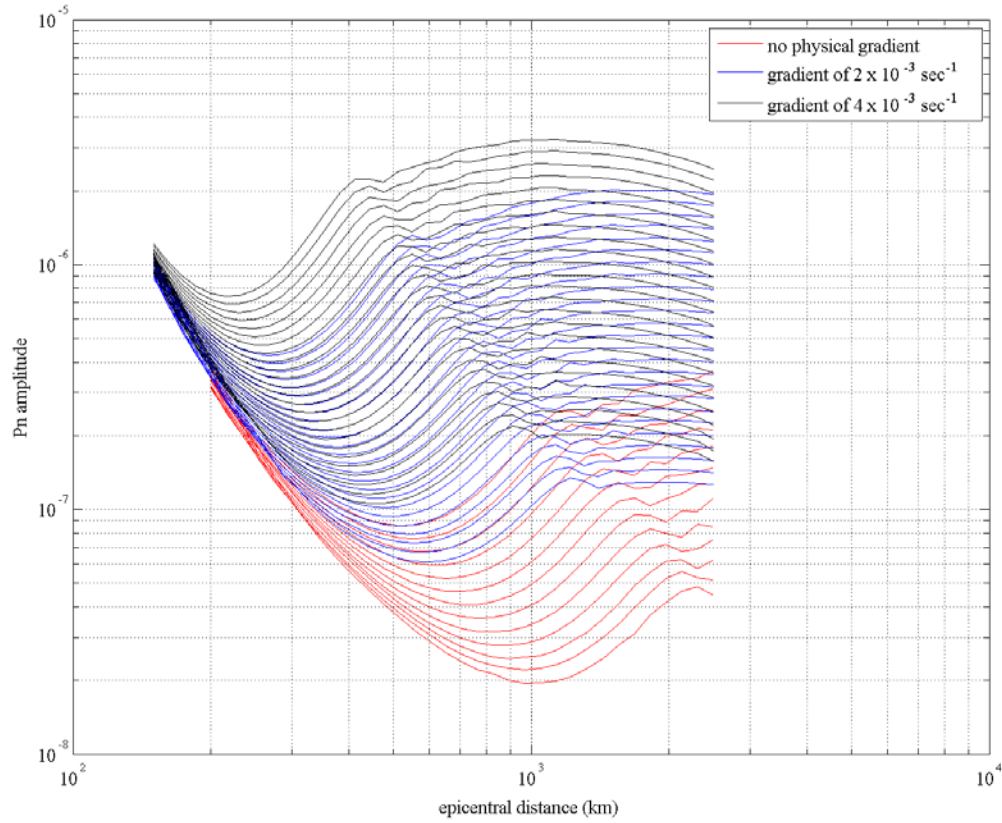


Figure 4. *Pn* amplitude versus distance curves similar to Figure 3, but for the Base Earth Model (red curves, for no physical gradient in the lid) and for two models with mild positive gradients in the mantle lid. *The suite of curves for each case corresponds to frequencies ranging from 0.75 Hz (lowest curve) to 12 Hz (highest curve).* From Avants *et al.* (2011).

***Pn* Spreading Sensitivity to Lateral Mantle Velocity Volumetric Heterogeneity**

In Avants *et al.* (2011), we explored the effects of lateral heterogeneity in the mantle lid velocity structure on *Pn* spreading using a 2D fourth-order finite-difference code (Xie and Lay, 1994). We included random lateral volumetric velocity fluctuations characterized by RMS velocity and varying horizontal and vertical averaging functions with different length scales in the Model. This allowed us to consider 2D random heterogeneity models like those shown in Figure 5.

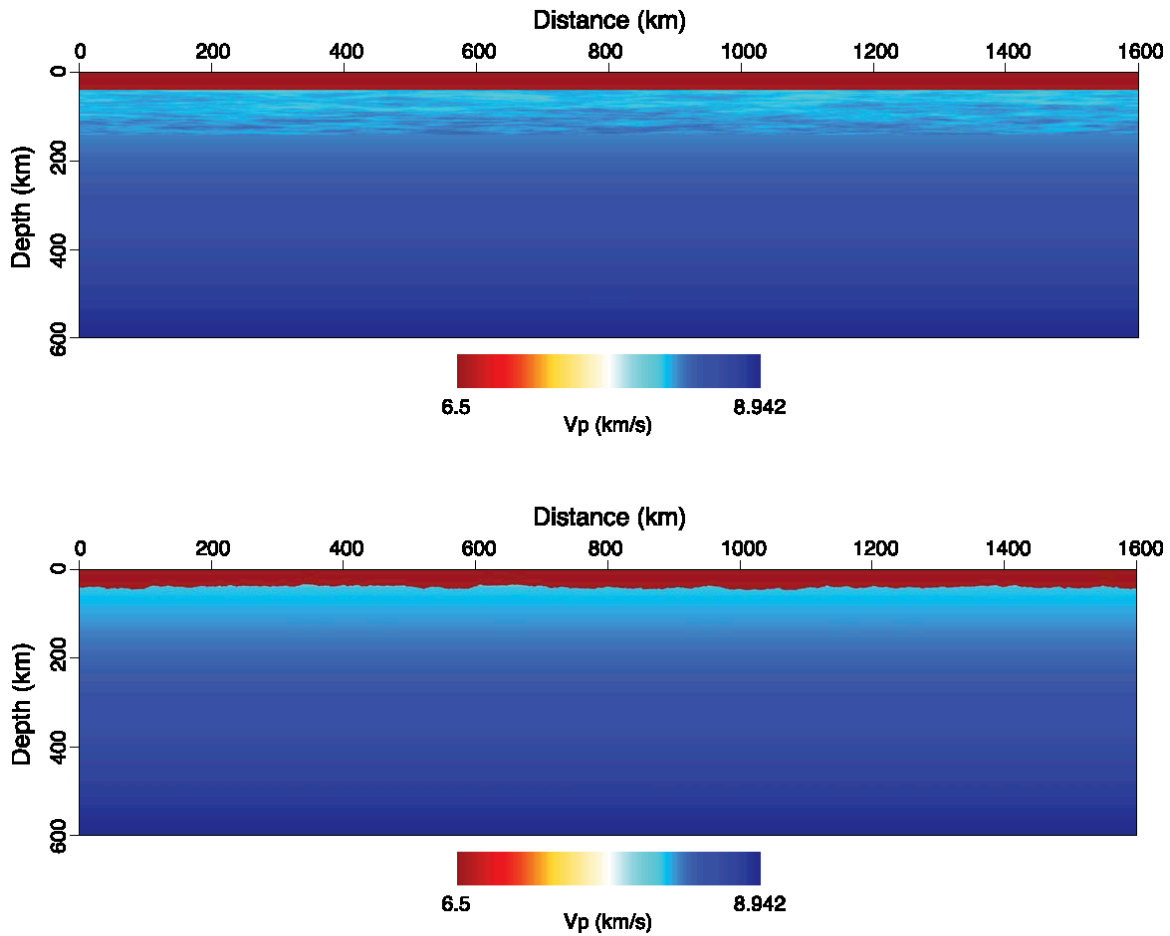


Figure 5. Visualizations of 2D velocity model with (top) 0.5% (rms) P -velocity heterogeneity in the upper one hundred kilometers of the mantle lid, and (bottom) exponential 3% (rms) roughness of the Moho with 40 km scale averaging length. *The background model is the EFT version of the Base Earth Model, so there is a slight positive velocity gradient across the crust and mantle. From Avants et al. (2011).*

The 2D finite-different modeling approach cannot achieve the very high frequencies of the 1D wave-number integration method, as the synthetics are limited to about 1 sec dominant period. Analysis of effects of random heterogeneity requires a statistical sampling of the effects associated with different realizations of the random velocity parameters. Many models have been run for various statistical properties of the mantle lid structure, with complete synthetic seismograms being computed.

Figure 6 shows the synthetic Pn amplitudes for ensemble averages of 5 realizations each for variable heterogeneity aspect ratios and rms velocity fluctuations for structures like that at the top in Figure 5, directly compared to the result for the Base Earth Model.

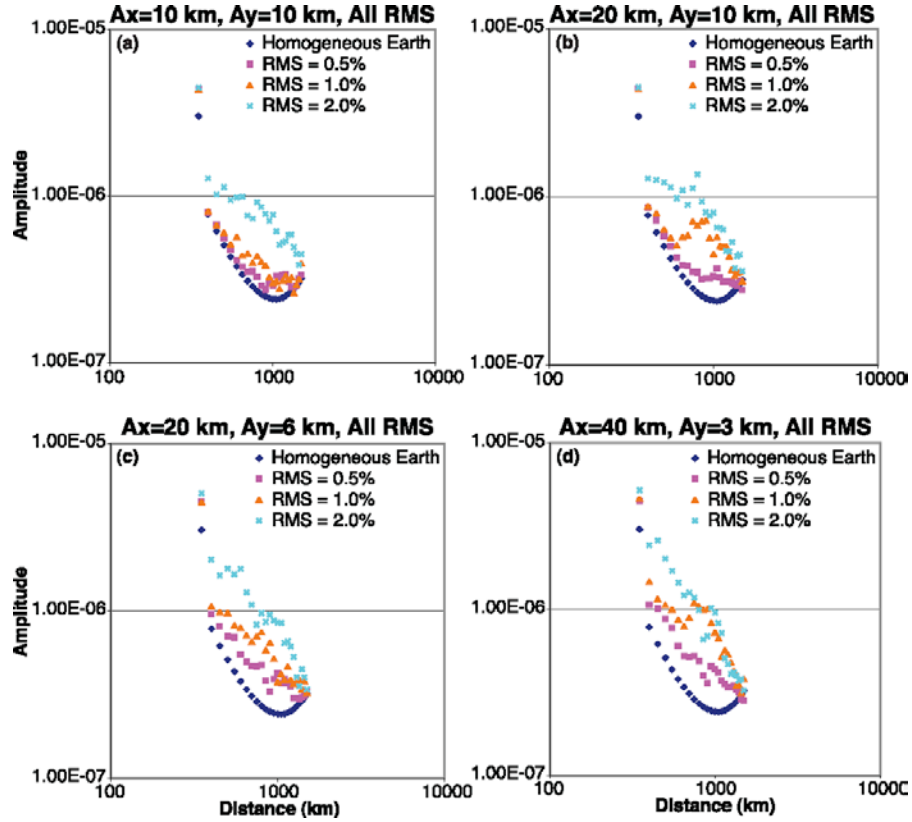


Figure 6. Ensemble-averaged P_n amplitudes as a function of distance for all configurations of random volumetric mantle heterogeneity simulated. P_n amplitude for the BEM (diamonds) are compared to models with 0.5% RMS (squares), 1.0% RMS (triangles), and 2% RMS (X's) V_p fluctuation for horizontal (A_x) and vertical (A_y) averaging lengths of (a) $A_x = 10$ km, $A_y = 10$ km (isotropic); (b) $A_x = 20$ km, $A_y = 10$ km; (c) $A_x = 20$ km, $A_y = 6$ km; and (d) $A_x = 40$ km, $A_y = 3$ km. Each value is the average of 5 realizations with different seed kernels.

An interesting behavior in Figure 6 is that the presence of velocity fluctuations affects the basic shape of the spreading, and in some cases it could be represented well by a power-law type behavior at this frequency (~ 1 Hz). This suggests that the 1D spreading behavior is rather delicate, with heterogeneity disrupting the specific interference that gives rise to the complex shape. As the strength of the velocity functions increases, there is progressive reduction of curvature of the amplitude-distance trend, and the overall amplitude behavior becomes increasingly power-law like. We emphasize that these simulations are 2D, are very bandlimited so frequency dependences is not known, and have prescribed velocity heterogeneity spectra. Whether they represent, or even approach the prevailing situation in the mantle lid is an open question and constraints can only come from observed data. In addition, more accurate modeling will require broadband 2D and 3D simulations. Nevertheless, the results demonstrate the effects of strong velocity heterogeneity on P_n geometric spreading.

***Pn* Spreading Sensitivity to Lateral Moho Topography**

While volumetric heterogeneity is expected to result from geological processes during crustal formation and evolution, the same is true for Moho irregularities on multiple scales. *Pn* and *Sn* interactions with the Moho near the source and receiver as well as throughout the propagation and whispering gallery development provide sensitivity to the Moho roughness. Avants et al. (2011) parameterized 2D exponential (Figure 5) and Gaussian statistical irregularities in the Moho depth to explore the effects of random structures, along with simple step-like structure in the Moho.

The exponential model is much richer in small-scale structure and produces longer enduring coda than the smoother Gaussian model, but the overall behavior of the models is similar for the 1 sec dominant period (Figure 7). For an 80 km horizontal averaging function the amplitude decay effects become significant for 5% RMS heterogeneity in the depth of the Moho. There is only minor sensitivity to the choice of horizontal averaging function for values larger than 40 km for a given statistical model.

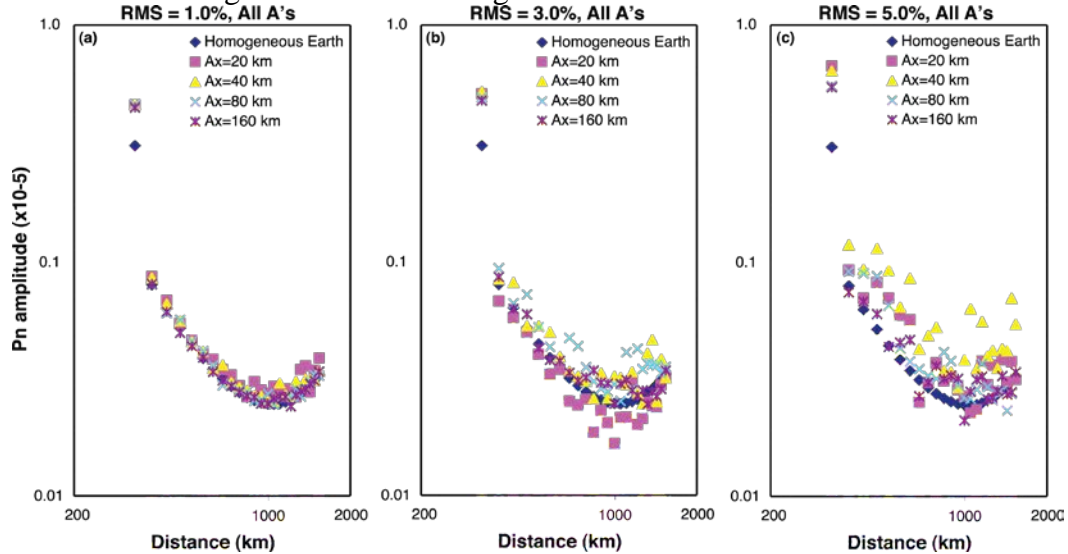


Figure 7. Ensemble-averaged *Pn* amplitudes plotted as a function of distance for all configurations of random Moho topography heterogeneity, grouped by percent RMS depth fluctuation. *Pn* amplitude for the BEM (diamonds) are compared to horizontal averaging length scales of 20 km (squares), 40 km (triangles), 80 km (X's), and 160 km (asterisks), for percent RMS depth fluctuations of (a) 1%; (b) 3%; and (c) 5%. From Avants et al. (2011).

***Pn* Spreading Model Constrained with Observed Data**

Yang (2011) evaluated the performance of Equation (2) in correcting observed *Pn* amplitudes in Asia. Figure 8 shows the 1-Hz *Pn* amplitudes after source and geometric-spreading correction using Equation (2). The figure shows that Equation (2) provides good spreading correction (leaving a linear trend in log amplitude versus distance) only over a limited distance range between about 860 and 1400 km. Outside this range,

corrected amplitudes exhibit undesirable variations (flattening and roughness) relative to a constant decay rate that could be expected for average attenuation of Pn .

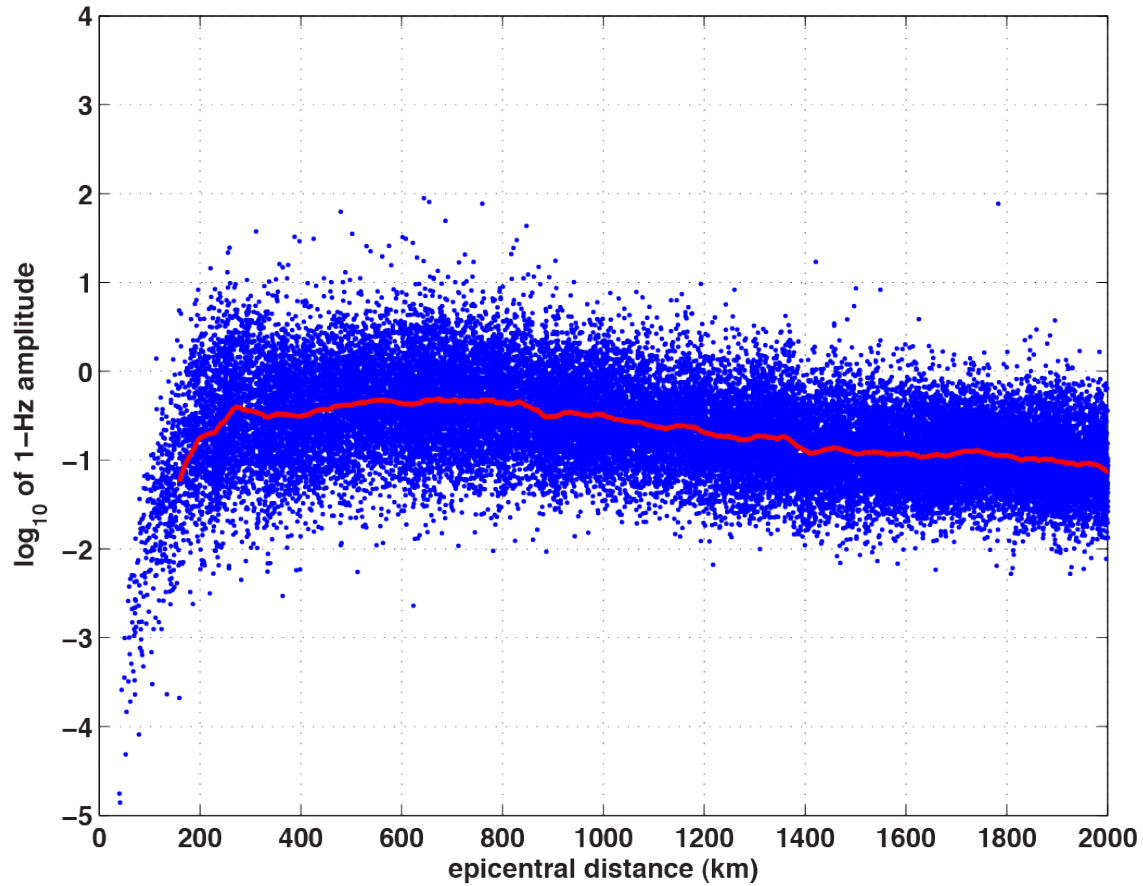


Figure 8. 1-Hz Pn amplitudes after source and geometric-spreading correction using the model developed by Yang et al. (2007). *The red line is the 400-point moving average showing the decay trend of the data.*

To better represent Pn spreading, Yang (2011) developed a method to construct observation-based and region-specific Pn spreading models. In his method, the average Pn Q at different frequencies is calculated from source and spreading (using Equation (2)) corrected Pn amplitudes. These Q values are then used to correct raw Pn amplitudes for attenuation. The resulting amplitude residuals are then fit with an observation-constrained spreading model. The Pn spreading model that Yang (2011) developed for Asia performs much better, resulting in a set of spreading-corrected amplitudes that have a constant distance decay slope for a wide distance range from 150 km to 1600 km (Figure 9).

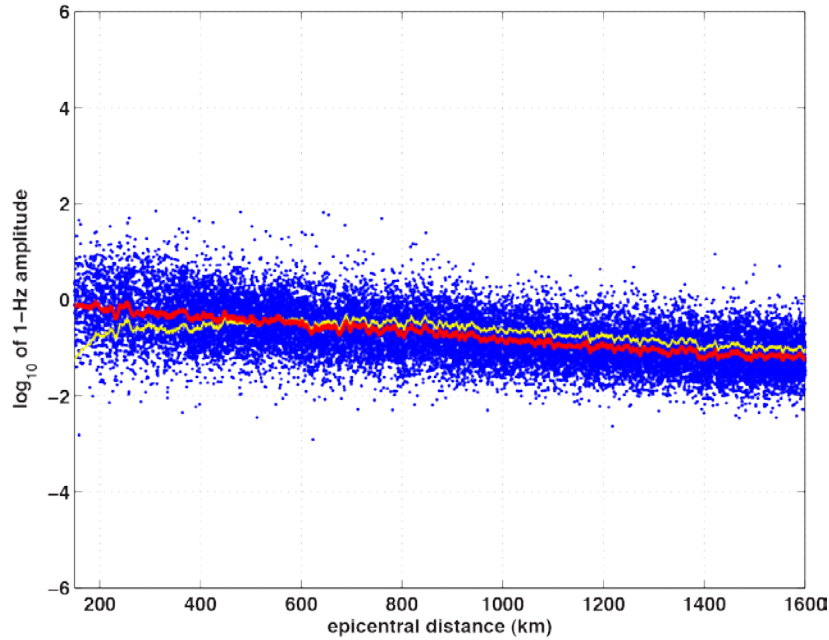


Figure 9. 1-Hz P_n amplitudes after source and geometric-spreading correction using the new model developed by Yang (2011). The red line is the 400-point moving average showing the decay trend of the data. The yellow line is the same as the red line in Figure 8.

The Effect of Geometric Spreading on Attenuation Determination

The tradeoff between geometric-spreading and attenuation makes it difficult to accurately estimate one parameter if the other parameter is not well constrained. The problem is particularly acute for P_n and S_n due to reasons discussed above. As a result, an accurate spreading relationship must be estimated, even for individual paths, in order to develop reliable 2D attenuation models used in amplitude corrections for discrimination and yield estimation.

To demonstrate the advantage and utility of a physics-based spreading model over traditional power-law model, Figure 10 compares the measured 1-Hz P_n amplitudes with the spreading model of Yang et al. (2007) and a power-law model. The figure shows that the Yang et al. (2007) model has a consistently slower decay rate than the data toward long distances, which is desirable if progressive attenuation occurs to produce the data trend over a large range of distance (yellow line). The power-law model, on the other hand, decays faster than the data toward long distances, which would result in a negative Q when trying to match the data behavior.

Figure 11 demonstrates this, showing examples of Q estimates obtained using either the model of Yang et al. (2007) or the power-law model for multiple frequencies. The model of Yang et al. (2007) yields reasonable Q values at all frequencies whereas using the power-law model results in either negative or extremely large Q values. These examples show that even though the model of Yang et al. (2007) is not optimal, it provides better

spreading corrections, due to its physics basis, than a power-law model, which corresponds to no known Earth structure.

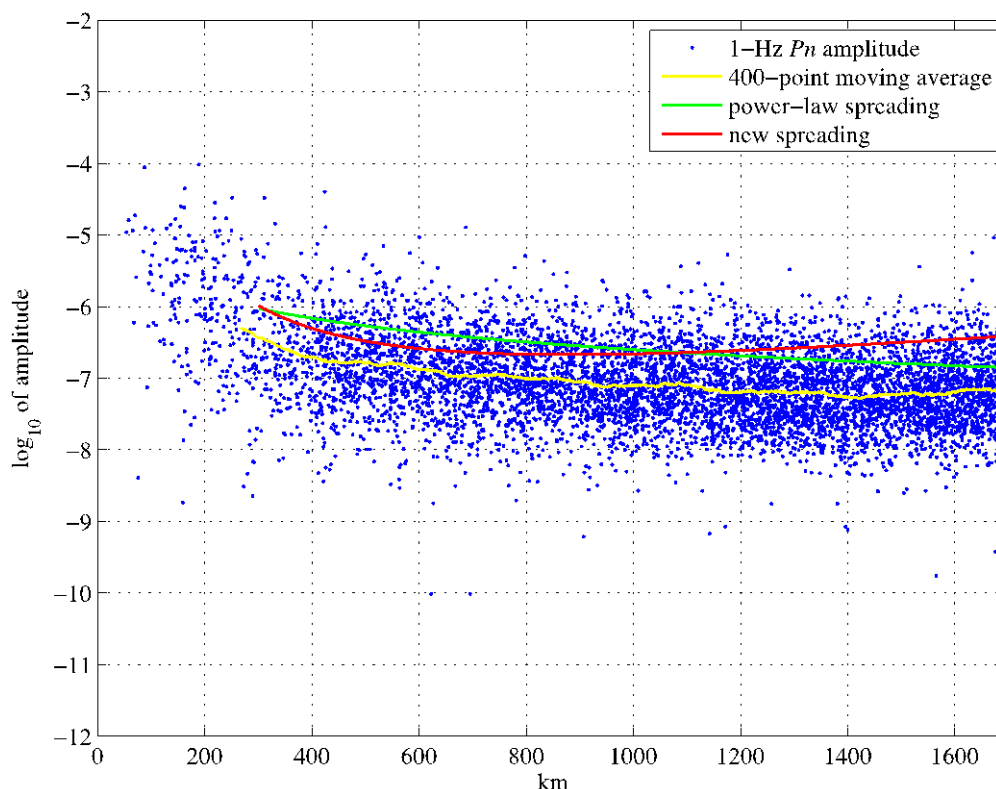


Figure 10. Comparison of 1-Hz P_n amplitude decay with decays predicted by a power-law spreading model and by the new spreading model of Yang *et al.* (2007). The yellow line is the 400-point moving average of the P_n data points to more-clearly delineate the amplitude-decay trend.

The foregoing review of accomplishments and enhanced understanding of geometric spreading for P_n (all attributes hold for S_n as well) indicates that reliable models of attenuation can be obtained only if reliable geometric spreading is computed for specific regional structure. Thus, a strategy for determining regional structures with observationally-constrained mantle-lid velocity gradients is needed.

The strategy of regional seismic travel time (RSTT) model parameterization advanced by Myers *et al.* (2010) adopts a geographic node description of crustal and upper mantle models, where the mantle portion is parameterized by a linear P-wave velocity gradient. This parameterization is very similar to that of the Base Earth Model used in the P_n and S_n geometric spreading calculations of Yang *et al.* (2007) and Avants *et al.* (2011) (Figure 12). Myers *et al.* (2010) used regional P_n travel times to develop a tomographic model of P_n velocity variation and mantle-gradient variation in the mantle lid (Figure 13). While the parameterization is not explicitly intended to predict amplitude behavior, nor are the resulting velocity models believed to be accurate in each case, the models can be used as a starting point to explore amplitude behavior.

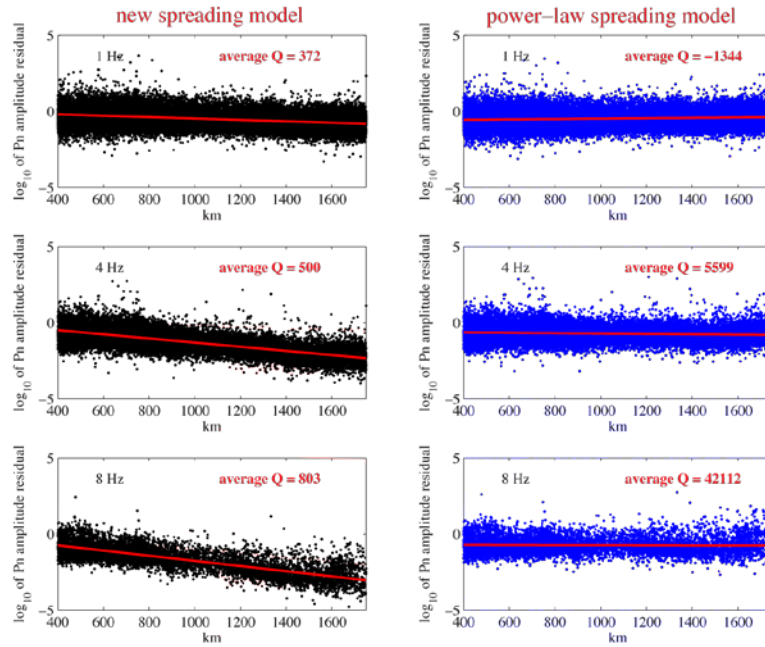


Figure 11. Comparison of average Q estimates from Pn amplitudes corrected for source and geometric-spreading effects using different spreading models. Q estimates at 1, 4 and 8 Hz are compared.

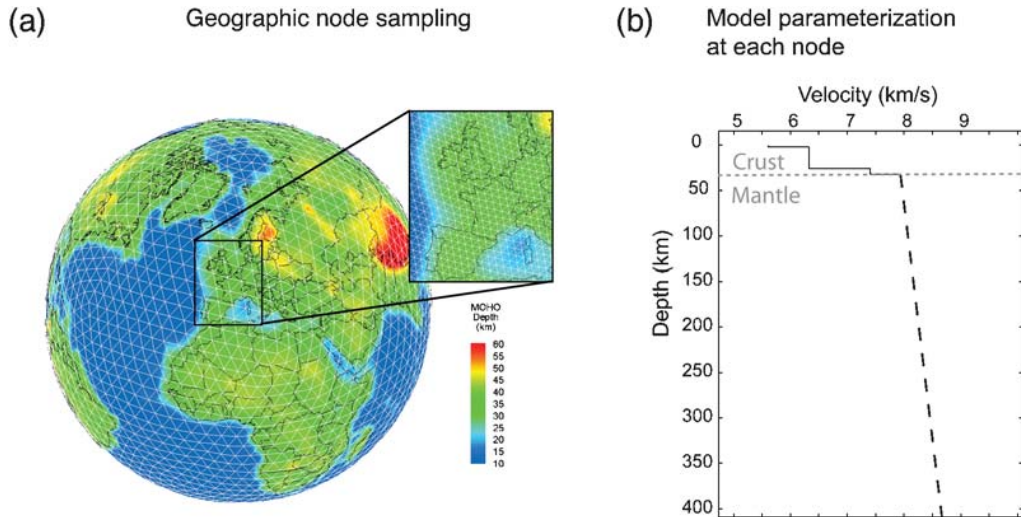


Figure 12. Global model parameterization. (a) An example tessellation with approximately 5° grid spacing. The inset shows the 1° used in the study by Myers et al. (2010). Color indicates Moho depth of the starting model. (b) An example velocity vs. depth profile as defined at each node. The mantle portion of the profile is specified by the velocity at the crust/mantle interface and a linear gradient. From Myers et al. (2010).

Regional phase arrival times were used by Myers et al. (2010) to develop a tomographic model (Figure 13) for variation in velocity of the uppermost mantle and variation in the strength of the mantle gradient. This provides regional models that fit

travel times, but the precision of the velocity gradients in the mantle is impacted by scatter in the data, averaging of nodes in a given region, and lack of resolution of curvature of P_n travel times. While the parameterization is not explicitly intended to predict amplitude behavior, the models can be used to do so.

We use RSTT derived models and associated travel time data, with corresponding regional phase amplitude measures as a function of frequency to evaluate use of travel time models as first-order structures for computing regional geometric spreading corrections (thereby having unified model frameworks for travel time and amplitudes), and as a starting point for revision of the models guided by observed amplitude behavior that is not well matched.

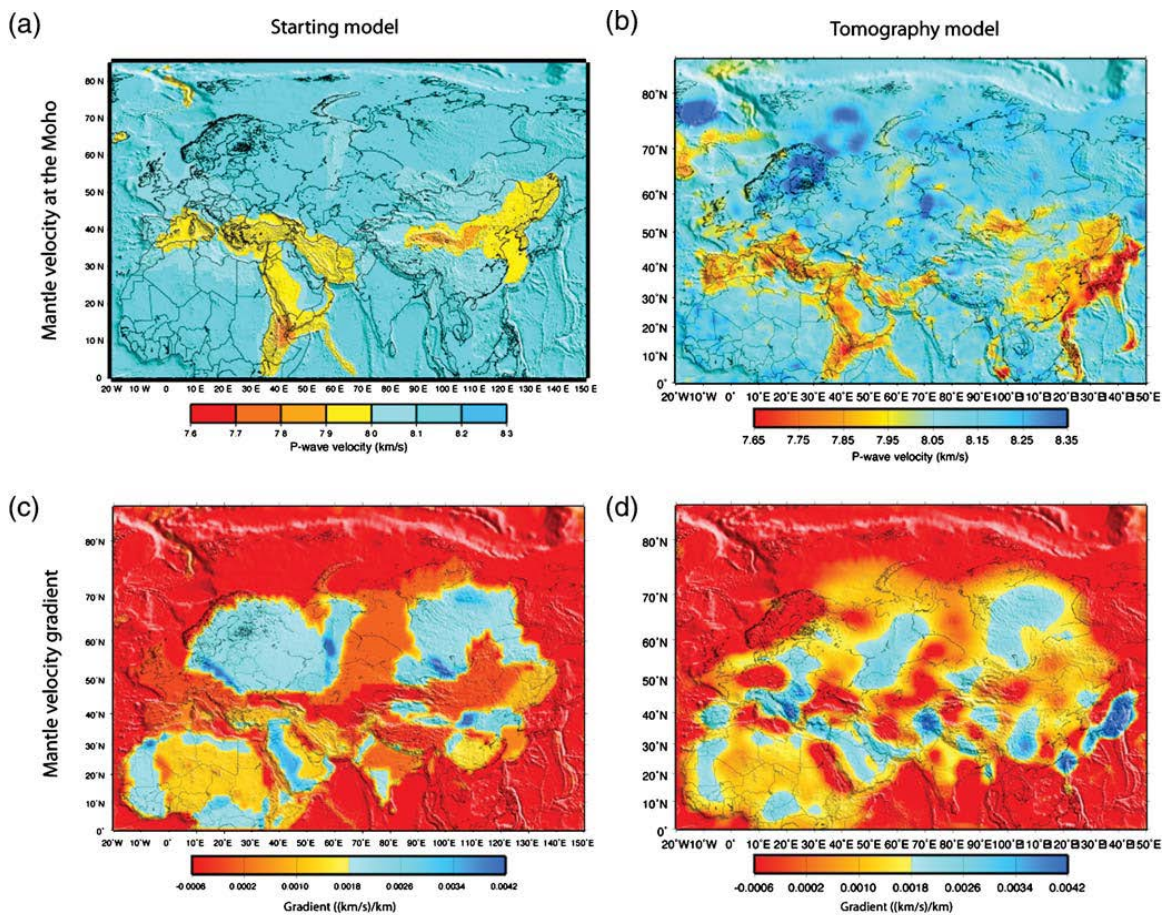


Figure 13. Comparison of starting and RSTT models. (a) Velocity below the Moho for starting model and (b) RSTT model. (c) Mantle gradient (km/sec/km) for starting model and (d) RSTT model. *From Myers et al. (2010).*

4. RESULTS AND DISCUSSION

Extending the bandwidth of 2D finite-difference calculations for large-distance Pn synthetics was one of the initial priorities. The fourth-order code used by Avants et al. (2011) was adapted to and tested on our cluster, and stable P-SV and SH calculations were achieved for ranges of up to 1000 km and frequencies up to 10 Hz, for models with a flat free-surface and laterally varying structure, either with or without small-scale statistical heterogeneity being included. This enables examination of Pn geometric spreading behavior in laterally varying 2D structure over broader bandwidth than in prior work. Figure 14 shows wavefield snapshots for simple 1D structures out to ranges of 900 km. These models have either constant velocity or linear gradients in the mantle lid.

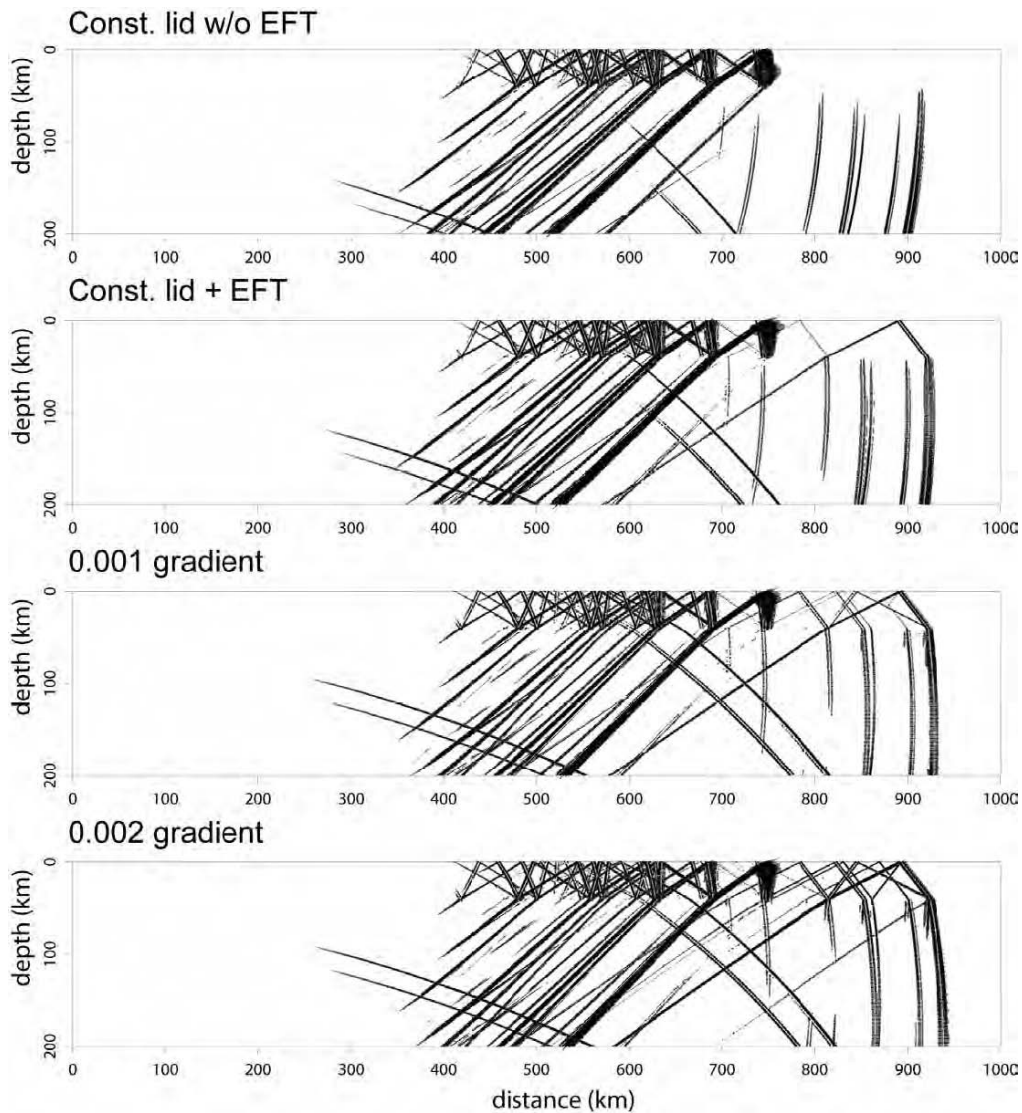


Figure 14. Snapshots of wavefields computed for 1D structures (constant lid gradient is w/o EFT) using the enhanced 2D finite-difference code implementation.

Corresponding synthetic seismogram profiles are shown in Figure 15, with the amplitudes being clipped for the very large amplitude direct Pg arrivals at closer distances to allow the Pn signal to be seen clearly. The reduction velocity is 8.1 km/s, equal to the constant mantle velocity layer in the BEM case with no earth-flattening.

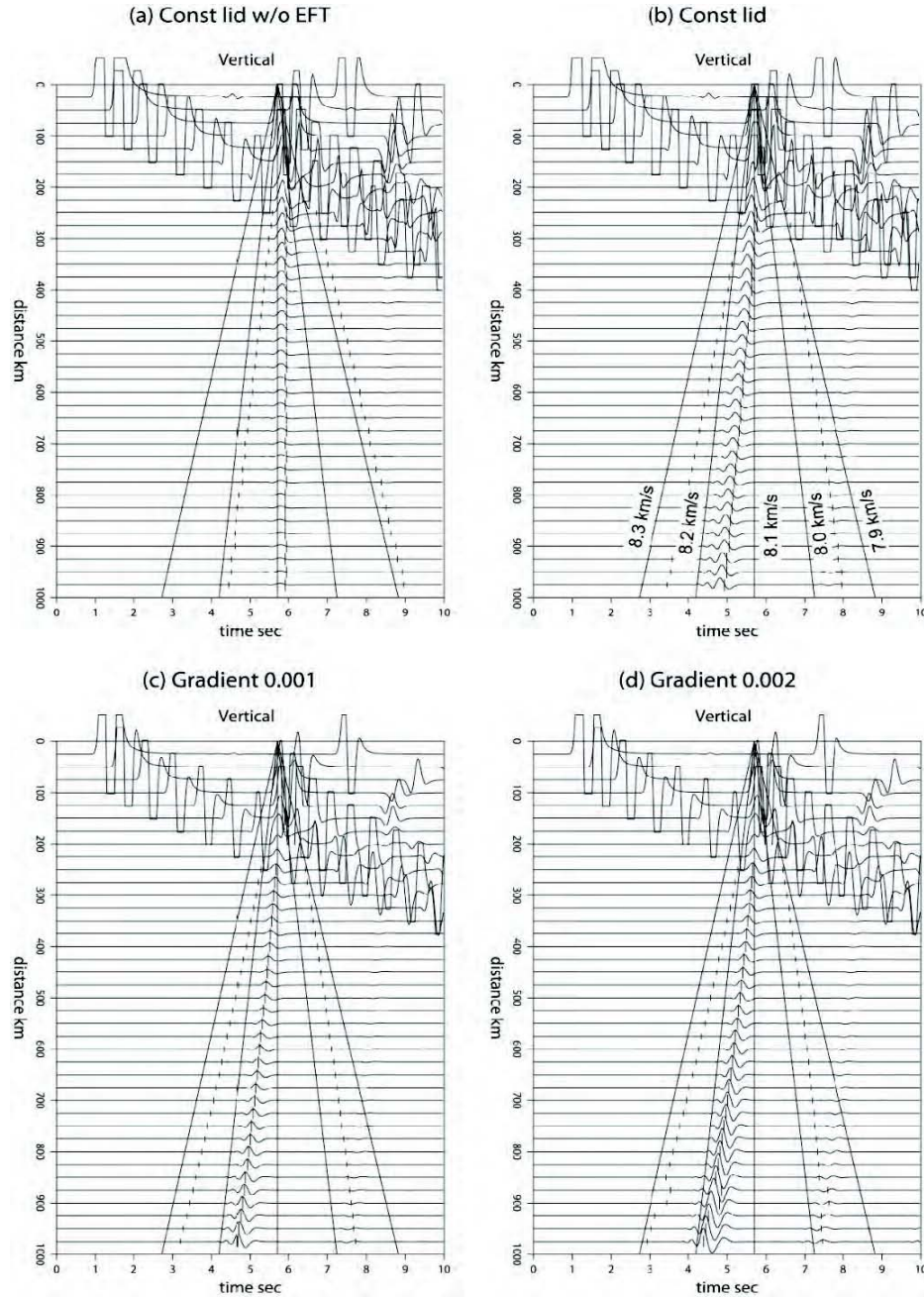


Figure 15. Vertical component synthetic seismograms computed by the 2D finite-difference code plotted with a reduction velocity of 8.1 km/s, which is the constant lid velocity in the basic Earth model (BEM). *Note the small waveform changes associated with positive lid velocity gradients and the systematic travel time curvature that would allow the velocity gradient to be resolved given sufficient regional observations.*

With the finite-difference code being fully tested and artifacts from grid dispersion being suppressed by very fine-model representation of the medium, we computed synthetics for 1D reference models (Figure 16) and 2D structures with slowly varying lateral changes in lid gradient. The goal was to establish the behavior of the frequency dependent Pn geometric spreading for simple models like those characterized by RSTT.

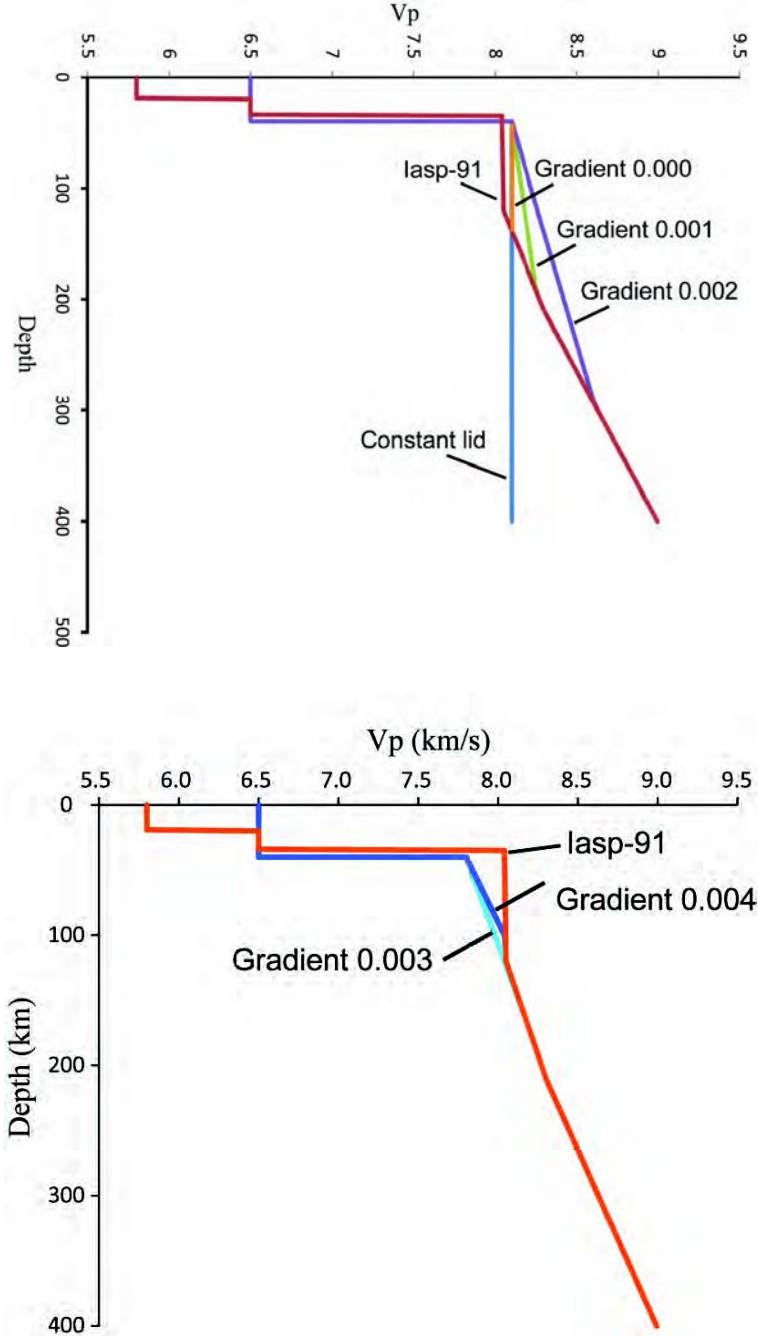


Figure 16. Reference velocity models considered as 1D structures or end-members of 2D structures with laterally varying mantle lid gradients for broadband Pn waveform computations up to 10 Hz at 1000 km distance. *At depth the models tie to the IASP-91 structure used as a reference in most tomography or location procedures.*

The travel time variations for these models are small, but potentially measureable, with picks from the synthetic waveforms being plotted versus distance in Figure 17. Potentially, regional observations could suffice to constrain the lid gradient, if the structure is laterally uniform, if crustal and site heterogeneity is accounted for, and if enough data are available to detect the subtle curvature of the travel time curves (versus simply mapping a different constant lid velocity value that would take out the linear trend in the time picks).

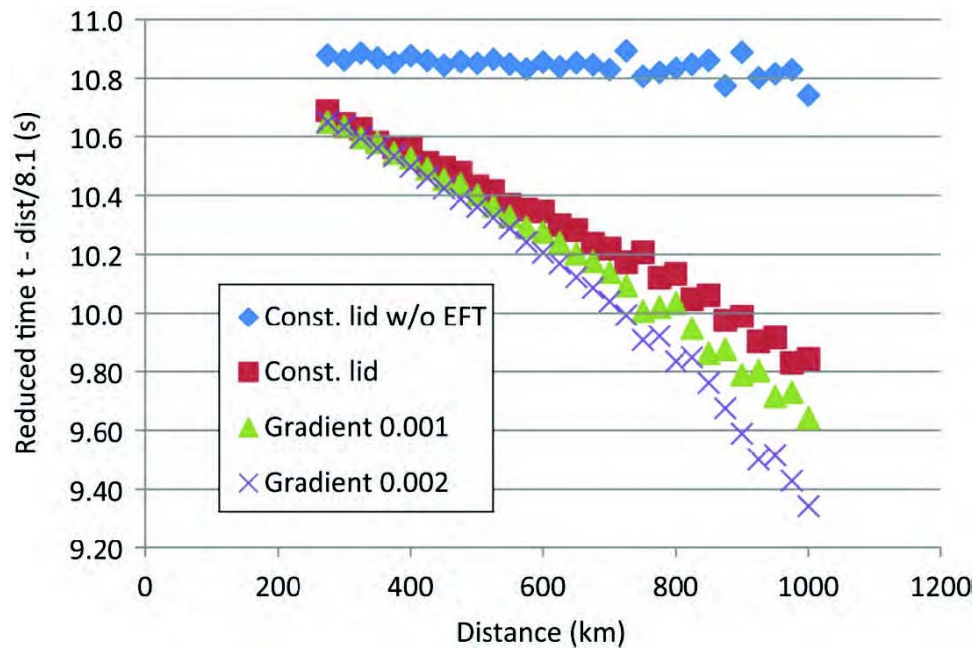


Figure 17. Arrival time picks from profiles of synthetics in Figure 15 displaying the weak curvature introduced by linear mantle lid gradients. *While the variations are subtle, given sufficient observations and laterally uniform structure, the mantle gradient can be constrained by Pn arrival time picks, providing velocity models that can be used for self-consistent regional amplitude spreading calculations.*

For the 1D models shown in Figure 16, we computed frequency-dependent geometric spreading amplitude decay out to 1000 km using the 2D model, correcting for behavior of a point-source versus a line-source. This provides the amplitude decay curves shown in Figure 18. These patterns are very similar to wavenumber-integration calculations for the same 1D velocity models computed in Avants et al. (2011) shown in Figure 4. The complex frequency-dependence of Pn, with minima in the amplitude-distance curves and rising amplitudes at larger distances, particularly for higher frequencies being evident for all structures with a positive gradient in the 1D flat earth structure. For lid gradients in excess of 0.002 sec^{-1} , the distance and frequency dependence are quite dramatic as shown before, with complex plateauing and oscillation of the high frequency components. Some of the large distance, high frequency behavior is not well-resolved, but very similar behavior is found for the completely independent frequency-wavenumber integration synthetics in Figure 4. Overall, these calculations provide a good level of confidence in the broadband Pn synthetics, and we proceed to consider results for 2D models.

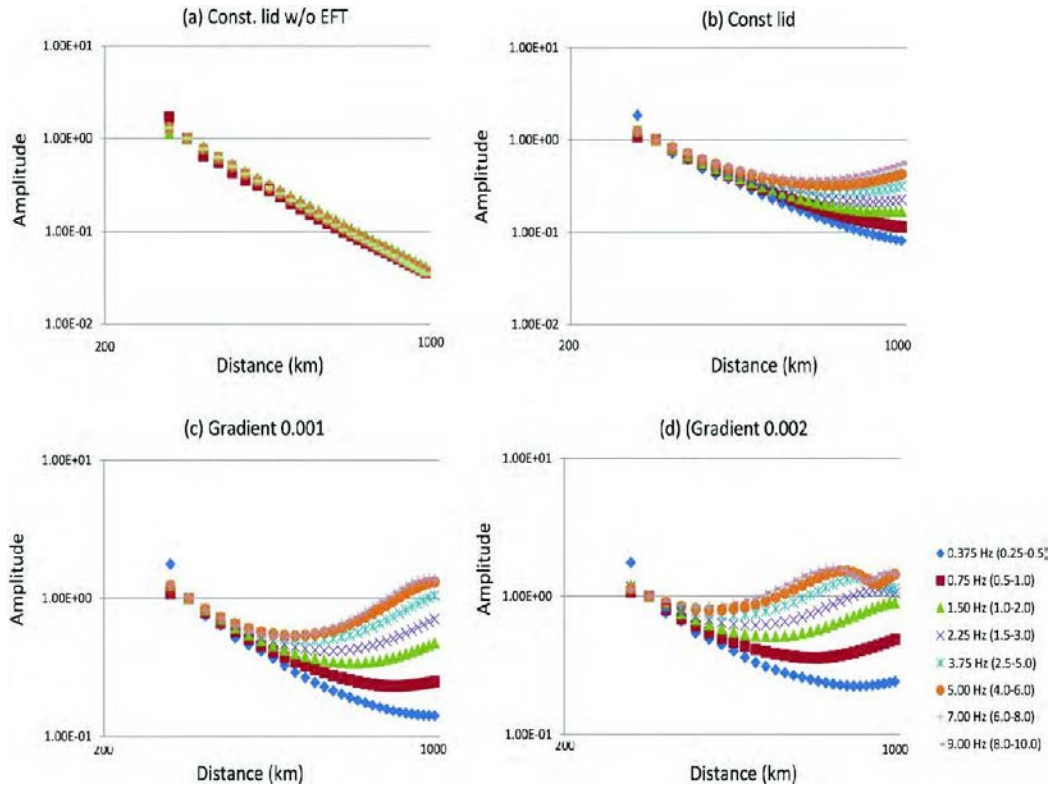


Figure 18. Pn amplitude decay as a function of narrowband frequency versus distance for models in Figure 16.

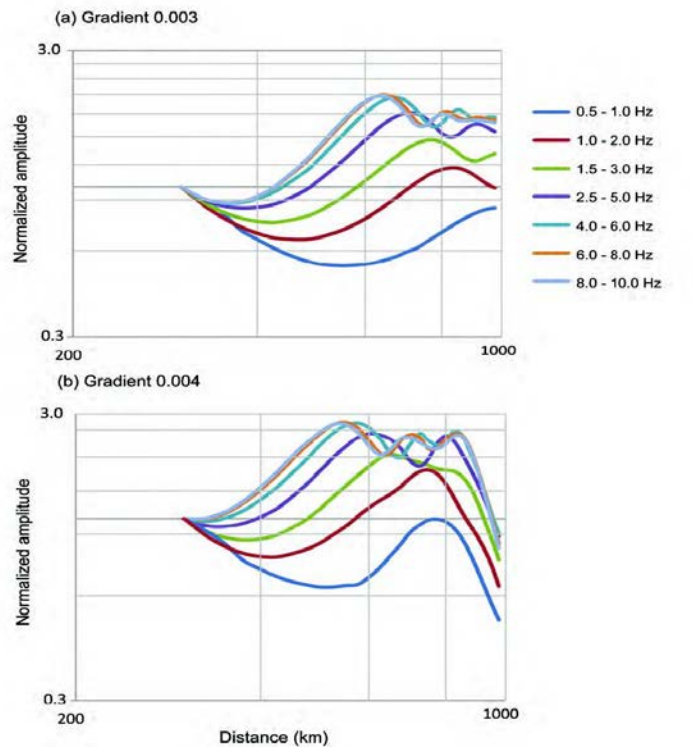


Figure 19. Pn amplitude decay as a function of narrowband frequency versus distance for models in Figure 16.

As an initial exploration of frequency-dependence of Pn spreading in laterally varying structures, we computed 2D synthetics for models where the mantle lid velocity gradient varied laterally. Example structures are shown in Figure 20. These approximate regions where average 1D structures differ beneath source and receiver regions. We computed cases for sources and receivers interchanged to explore asymmetry in the Pn behavior.

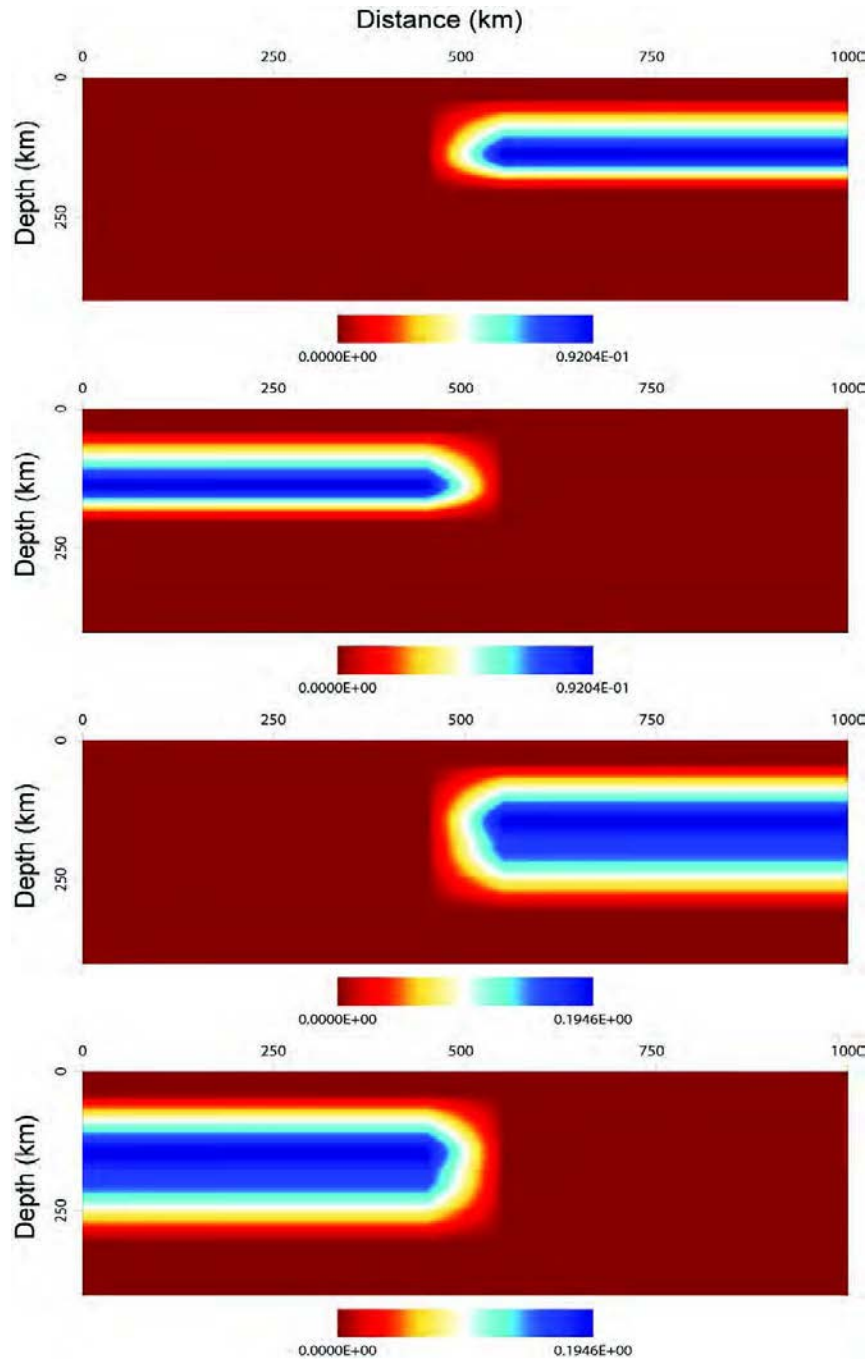


Figure 20. 2D velocity models with laterally varying mantle lid velocity gradients that vary beneath the source and receiver locations. *Finite-difference Pn synthetics were computed out to ranges of 1000 km and for frequencies up to 10 Hz.*

Amplitude distance curves are displayed for varying frequencies in Figure 21, showing the differences from 1D models with zero or constant velocity gradients and the 2D cases that have the source or receiver in regions with the two end-member 1D models.

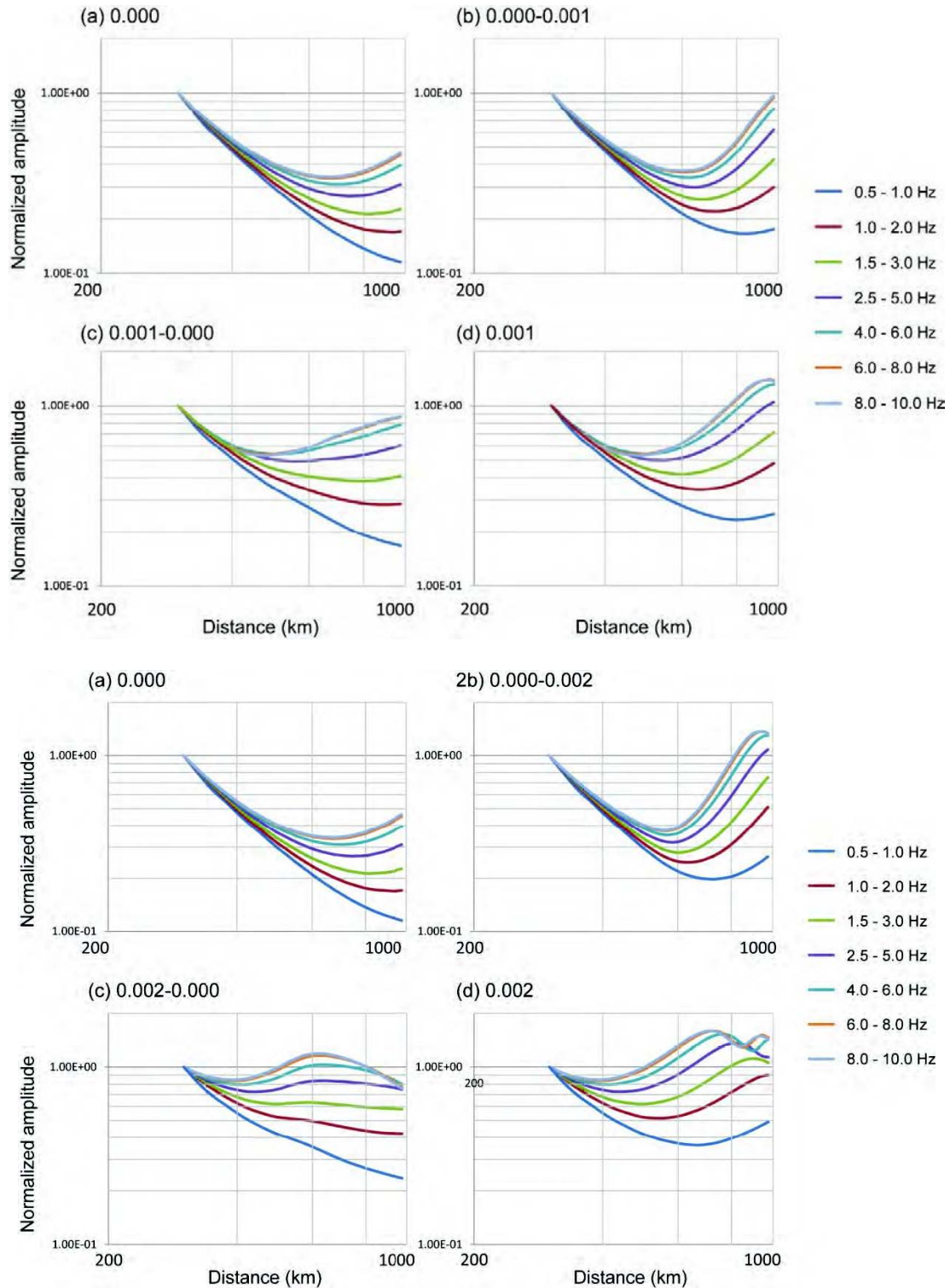


Figure 21. Pn amplitude versus distance for 1D (Figure 16) and 2D models (Figure 20) for varying bandpass center frequencies.

The clear tendency is for the Pn spreading along the path to be dominated by the source side structure at closer distances and the receiver side structure at longer distances, with overall pattern being very different when the direction on the path is reversed. This behavior places special emphasis on working toward path-specific corrections, as any regional average used for all paths in the region would clearly provide a poor approximation. The path averaging behavior is further emphasized in Figure 22, which shows the results for just a single frequency (3.75 Hz). Note the differences between the red and green curves, which are for simple interchange of the source and receiver positions. Further exploration of laterally varying models and addition of small-scale scattering structure will be pursued along with exploring 3D calculations using a one-way propagator approach.

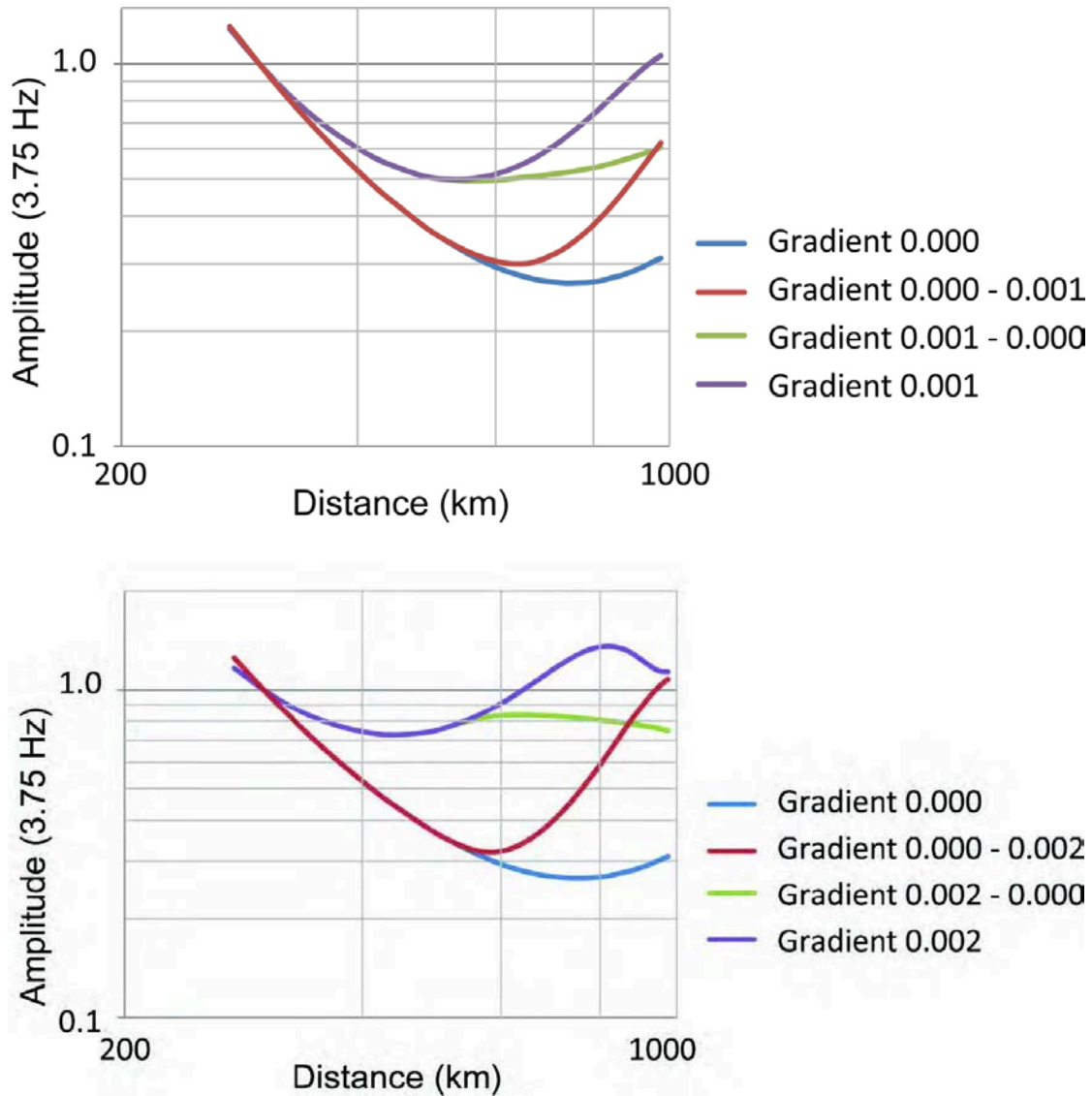


Figure 22. Pn amplitude versus distance for 1D (Figure 16) and 2D models (Figure 20) for a 3.75 Hz center frequency of a narrow bandpass. *The near-source velocity gradient is indicated first in each laterally varying calculation.*

In parallel with the computational effort, we have empirically examined the use of regionalized corrections for Pn amplitudes guided by RSTT regional velocity models and by empirical analysis of Pn data with the constraint of realistic spreading behavior as established by Yang (2011). Figure 23 displays the regionalization guided by RSTT models.

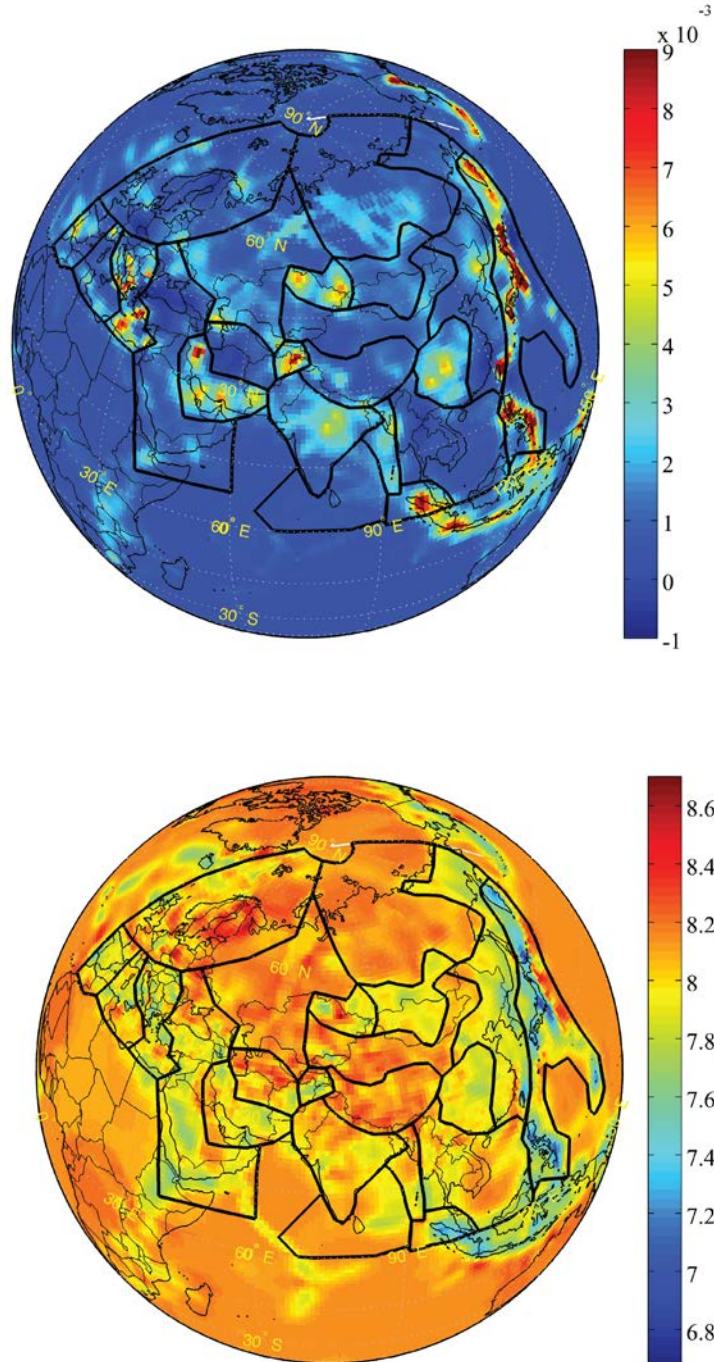


Figure 23. RSTT model lid velocity gradients (top) and average Moho P velocity (bottom) with a superimposed grid developed to define provinces of similar parameters.

The LANL database for Pn measurements (Figure 24) is used to extract signals and measured Pn amplitudes in varying passbands to define the sampling of regions (Figure 25) for which RSTT mantle lid gradient and/or average Moho velocity are relatively uniform.

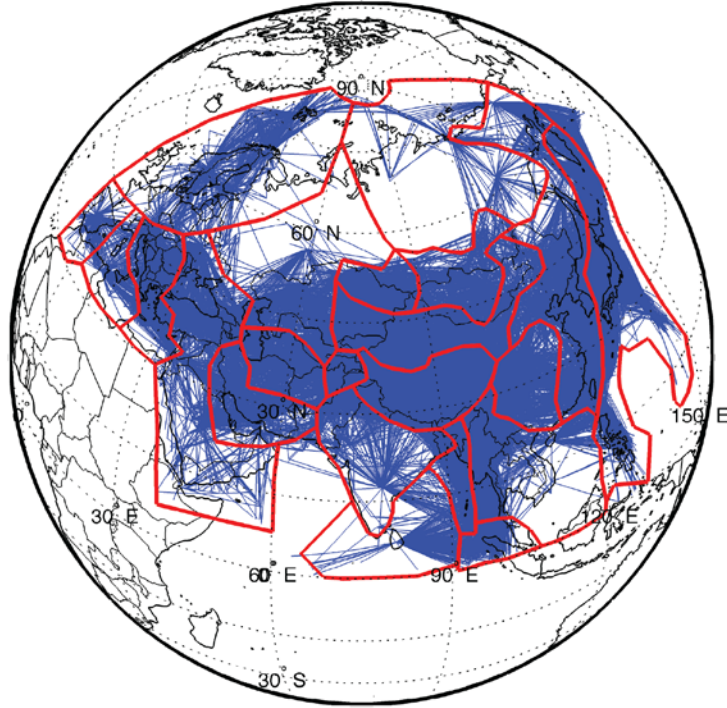


Figure 24. LANL Eurasian Pn data base coverage showing Pn paths sampling the RSTT-based regionalization.

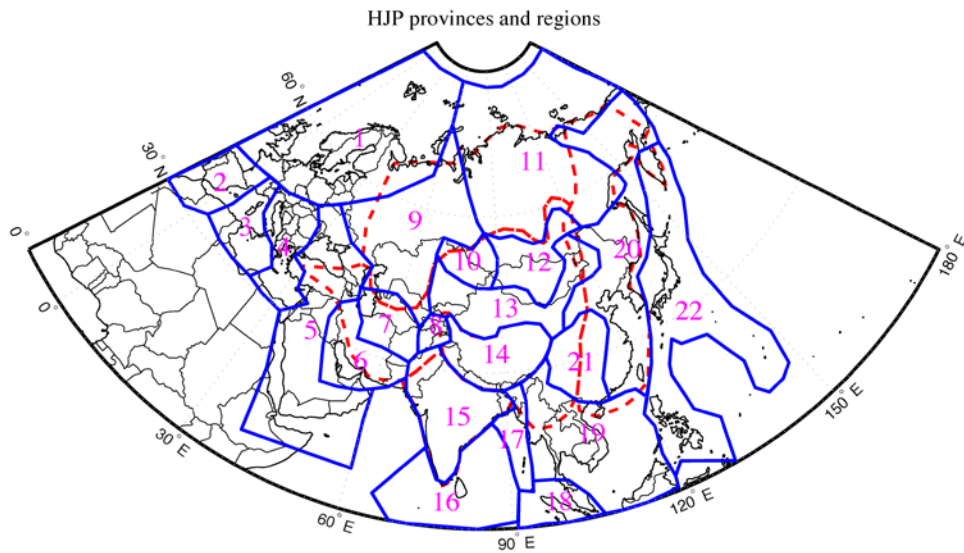


Figure 25. Regional numbering scheme for the RSTT-based subdivision. *Pn* observations in each region have been evaluated. Model spreading parameters for each RSTT structure have been determined.

For each region identified in Figure 25, we computed spreading behavior for a 1D average of the local RSTT model using wavenumber integration, and applied corresponding frequency-dependent geometric spreading corrections to the MDAC-corrected Pn observations for that region. We also applied simple power-law spreading corrections for a power of -1.1, and we determined region-specific spreading corrections following the procedure of Yang (2011). This gives three sets of corrected Pn data for each region. Plotting these sets of corrected Pn amplitudes (\log_{10}) as functions of distance, allows an estimation of the average Q for that region for each frequency. We display results for regions 4 and 13 (Figure 25) in Figures 26a,b and 27a,b, respectively.

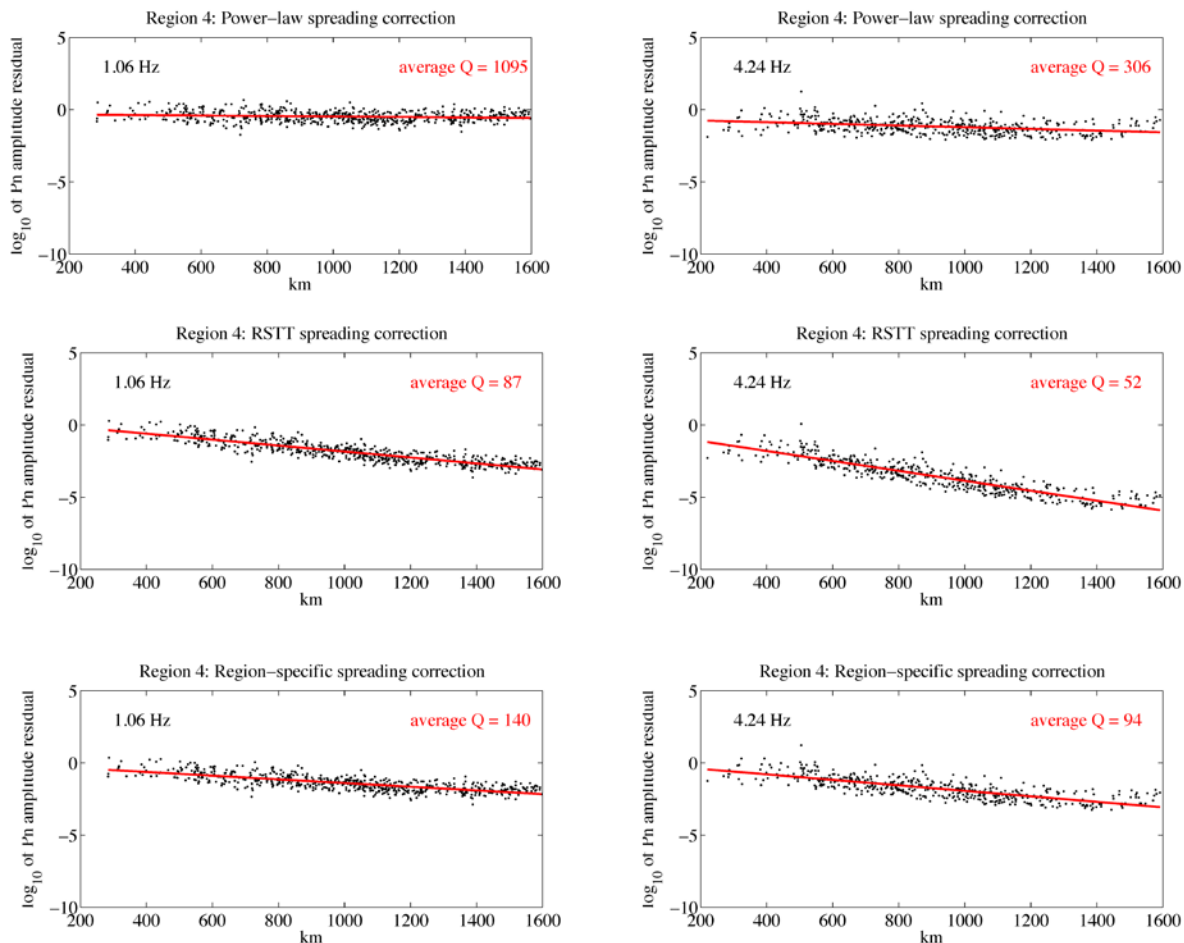


Figure 26a. Pn amplitudes versus distance for Region 4 with corrections using a power-law (top row), RSTT-based synthetic computations (middle row) or empirical region-specific corrections following the procedure of Yang (2011) (bottom row) for passband center frequencies of 1.06 Hz (left) and 4.24 Hz (right). *The measured average Q for each case obtained from the regression curve is indicated in the upper right.*

Each set of geometric spreading corrections results in relatively smooth linear amplitude versus distance trends that suggest a corresponding average Q for that frequency. But the Q values that are inferred vary dramatically, depending on the geometric spreading used.

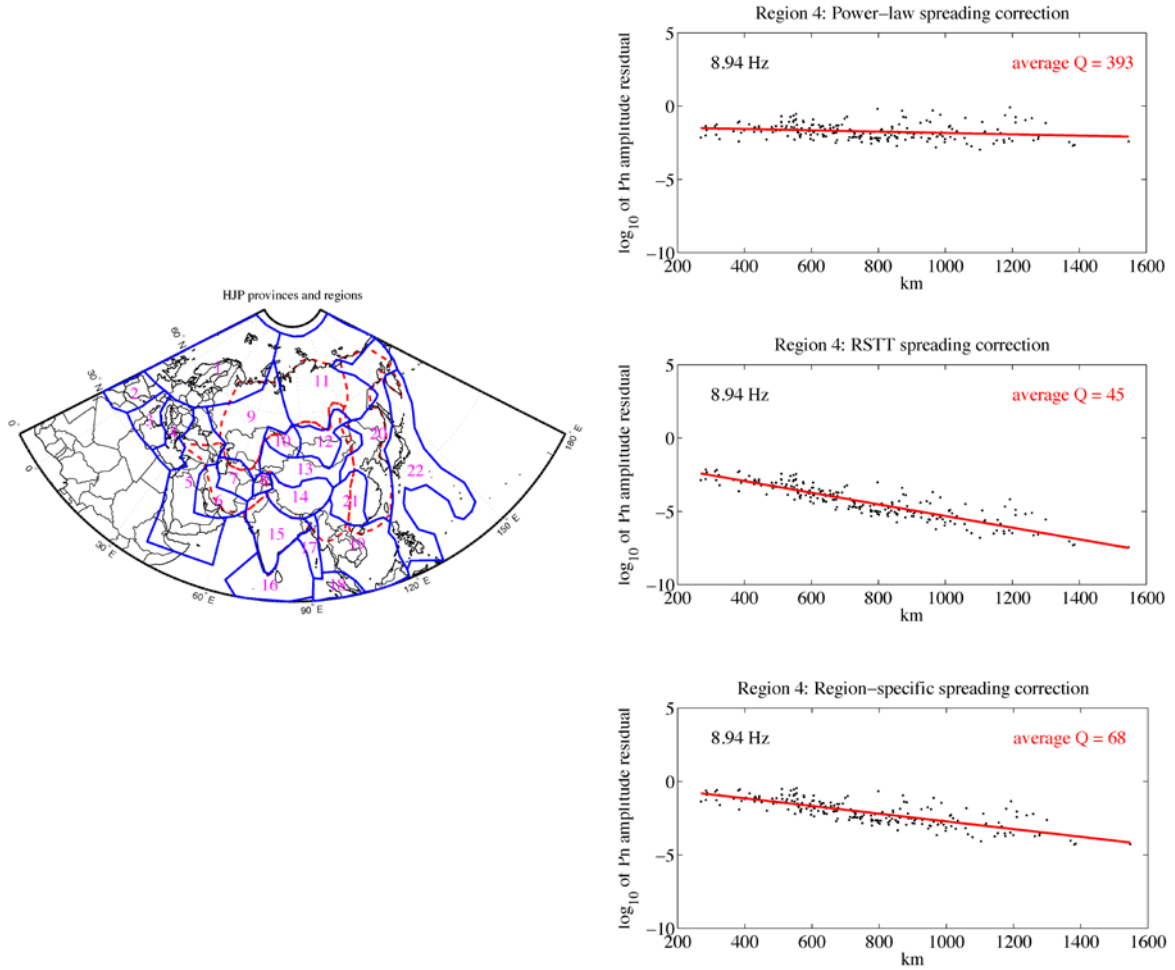


Figure 26b. Pn amplitudes versus distance for Region 4 (map inset) with corrections using a power-law (top row), RSTT-based synthetic computations (middle row) or empirical region-specific corrections following the procedure of Yang (2011) (bottom row) for passband center frequency of 8.94 Hz (right). *The measured average Q for each case obtained from the regression curve is indicated in the upper right.*

In general, as found by Yang et al. (2007) and Yang (2011), use of a ‘standard’ power-law spreading correction with an exponent of -1.1 that does not vary with frequency (and for which there is no specific known structure) gives high Q values in every case, and even negative Q value for Region 13 at 1.06 Hz. For Region 4, the RSTT velocity gradient is relatively high (0.0026 s^{-1}) while for Region 13 it’s average (0.0012 s^{-1}). In both cases, the addition of the Earth flattening transformation (EFT) gradient of 0.0013 s^{-1} gives positive velocity gradients that produce strong frequency-dependent Pn amplitude corrections. The data have somewhat less scatter and systematically lower Q values are inferred for each region using the RSTT based corrections. Q values that are 1.6-1.8 times higher than the RSTT-based results are found for corrections based on the region-specific spreading corrections following Yang (2011). The absolute values and the frequency-dependence of the attenuation parameters are more similar for the RSTT- and regional-based spreading corrections. For these regions there is no clear reduction in

scatter to favor a specific spreading model, but the Q values appear to be more reasonable for either of the frequency-dependent spreading corrections results. As long as the Q model for a given spreading model is used, total amplitude calculations will be reasonably similar. The main advantages of using a more appropriate local velocity model to process the amplitudes is that a more reliable Q model may be estimated and that could be valuable for application to full waveform modeling, for extrapolation to poorly sampled paths, and for overall self-consistency of event locations and amplitudes.

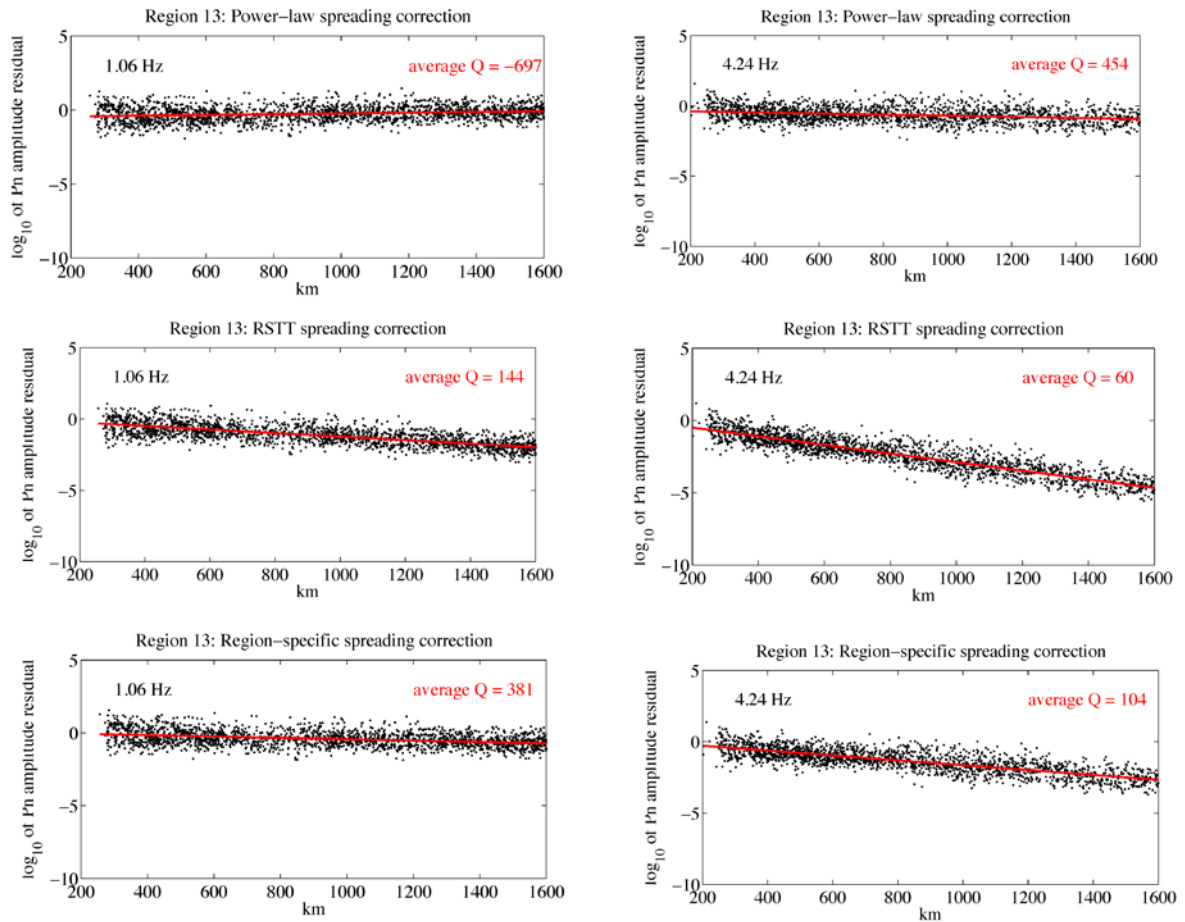


Figure 27a. Pn amplitudes versus distance for Region 13 with corrections using a power-law (top row), RSTT-based synthetic computations (middle row) or empirical region-specific corrections following the procedure of Yang (2011) (bottom row) for passband center frequencies of 1.06 Hz (left) and 4.24 Hz (right). *The measured average Q for each case obtained from the regression curve is indicated in the upper right.*

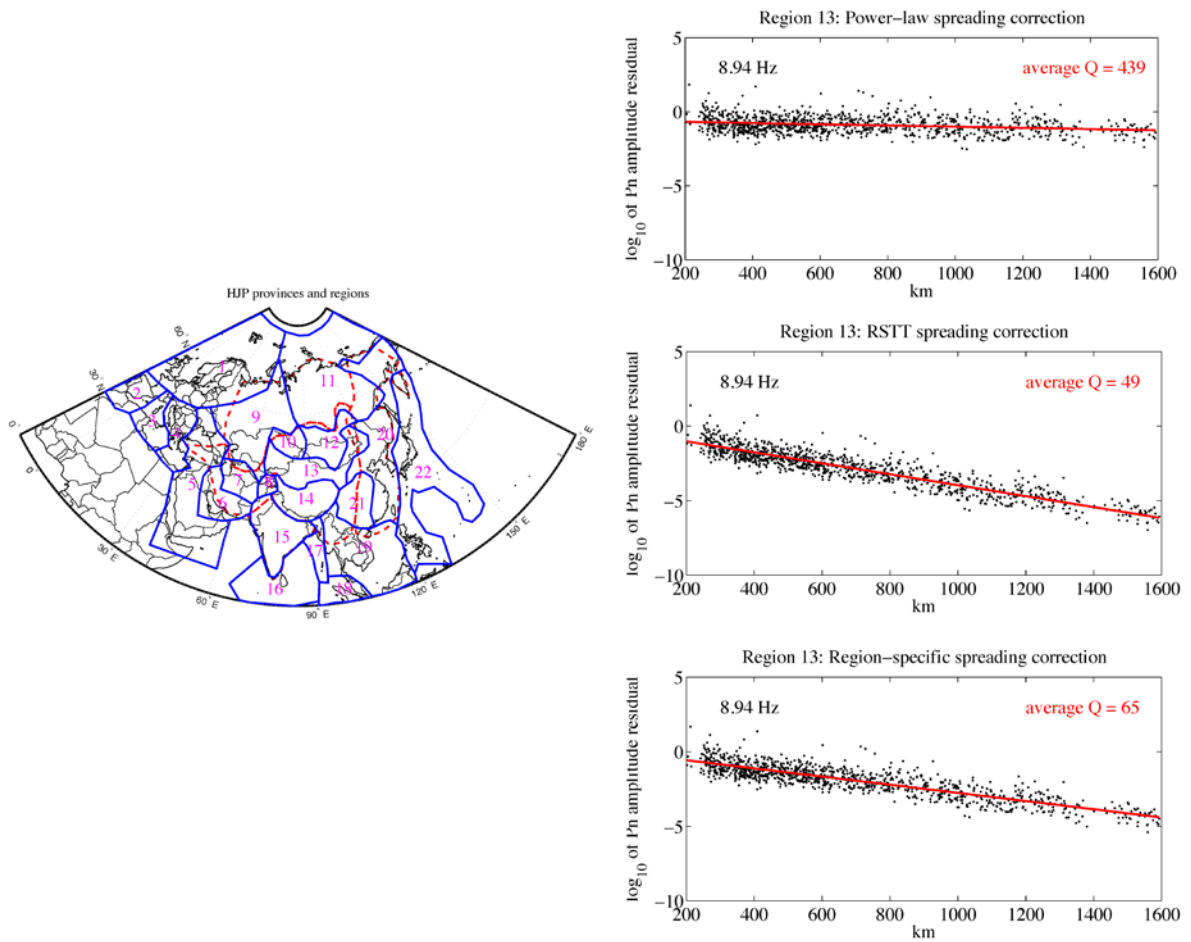


Figure 27b. Pn amplitudes versus distance for Region 13 (map inset) with corrections using a power-law (top row), RSTT-based synthetic computations (middle row) or empirical region-specific corrections following the procedure of Yang (2011) (bottom row) for passband center frequency of 8.94 Hz (right). *The measured average Q for each case obtained from the regression curve is indicated in the upper right.*

5. PRELIMINARY FINDINGS

New 2D computations of Pn geometric spreading have established that the amplitude variation is dependent on direction of the path and that complex frequency dependence is expected to have mixing of the near-source and near-receiver structures. This further weakens the rationale for using average power-law representations of the Pn (and Sn) geometric spreading. As the only structure that will result in a power law behavior for sure are those with negative critical gradients in the mantle lid (a possible, but likely very rare situation), we further support Yang's (2011) contention that a simple velocity model based correction, or an empirically grounded correction is a more sensible choice than a frequency-independent power law. We will explore some models with fine-scale heterogeneity to evaluate whether the tendency to smooth out the distance behavior for 1 Hz signals as found by Avants et al. (2011) holds for broadband Pn signals.

Application of regionalized Pn spreading corrections based on RSTT models (derived exclusively from regional travel time observations and velocity models) or regionalized fitting of attenuation models to data provide fairly similar $Q(f)$ estimates, much lower than those from constant power law spreading coefficient. While the choice of optimal spreading is not unambiguous in every case based on some measure of variance reduction in the model performance, the more reasonable attenuation parameters obtained using the RSTT or empirical spreading corrections suggest they are more reasonable than standard power law assumptions.

REFERENCES

- Aki, K. and P.G. Richards, 2002, Quantitative Seismology: Theory and Methods, University Science Books, 2002, ISBN 0-935702-96-2.
- Avants, M., T. Lay, X.-B. Xie, and X. Yang, 2011, Effects of 2D random velocity heterogeneities in the mantle lid and Moho topography on *Pn* geometric spreading, *Bull. Seism. Soc. Am.*, 101, pp. 126-140.
- Fisk, M.D., H.L. Gray, and G.D. McCartor, 1996, Regional discrimination without transporting thresholds, *Bull. Seism. Soc. Am.*, 86, pp. 1545-1558.
- Fisk, M.D., S.R. Taylor, and T. Lay, 2005, Modeling and empirical research on energy partitioning of regional seismic phases used for explosion monitoring, Proceedings of the 27th Seismic Research Review, pp. 539-549.
- Hartse, H.E., S.R. Taylor, W.S. Phillips, and G.E. Randall, 1997, A preliminary study of regional seismic discrimination in central Asia with emphasis on western China, *Bull. Seism. Soc. Am.*, 87, pp. 551-568.
- Kim, W. Y., V. Aharonian, A.L. Lerner-Lam and P.G. Richards, 1997, Discrimination of earthquakes and explosions in southern Russia using regional high-frequency three-component data from IRIS/JSP Caucasus Network, *Bull. Seism. Soc. Am.*, 87, pp. 569-588.
- Myers, S.C., M.L. Begnaud, S. Ballard, M.E. Pasyanos, W.S. Phillips, A.L. Ramirez, M.S. Antolik, K.D. Hutchenson, J.J. Dwyer, C.A. Row, and G.S. Wagner, 2010, A crust and upper-mantle model of Eurasia and North Africa for *Pn* travel time calculation, *Bull. Seism. Soc. Am.*, 100, pp. 640-646.
- Patton, H.J., 2001, Regional magnitude scaling, transportability, and Ms:mb discrimination at small magnitudes, *Pageoph*, 158, pp. 1951-2015.
- Richards, P.G. and W.-Y. Kim, 2007, Seismic signature, *Nature Physics*, 3, pp. 4-6.
- Sereno, T.J. and J.W. Given, 1990, *Pn* attenuation for a spherically symmetric Earth model, *Geophys. Res. Lett.*, 17, pp. 1141-1144.
- Taylor, S.R., 1996, Analysis of high frequency *Pn*/*Lg* ratios from NTS explosions and western U.S. earthquakes, *Bull. Seism. Soc. Am.*, 86, pp. 1042-1053.
- Taylor, S.R., M.D. Denny, E.S. Vergino, and R.E. Glaser, 1989, Regional discrimination between NTS explosions and western U.S. earthquakes, *Bull. Seism. Soc. Am.*, 79, pp. 1142-1176.
- Taylor, S.R. and H.E. Hartse, 1997, An evaluation of generalized likelihood ratio outlier detection to identification of seismic events in western China, *Bull. Seism. Soc. Am.*, 87, pp. 824-831.
- Walter, W.R., K.M. Mayeda, and H. Patton, 1995, Phase and spectral ratio discrimination between NTS earthquakes and explosions. Part I: Empirical observations, *Bull. Seism. Soc. Am.*, 85, pp. 1050-1067.
- Xie, J., 2002, Source scaling of *Pn* and *Lg* spectra and their ratios from explosions in central Asia: Implications for the identification of small seismic events at regional distances, *J. Geophys. Res.*, 107, B7, 10.1029/2001JB000509.
- Xie, X.B. and T. Lay, 1994, The excitation of *Lg* waves by explosions: A finite-difference investigation, *Bull. Seism. Soc. Am.*, 84, pp. 324-342.
- Yang, X., 2011, A *Pn* spreading model constrained with observed amplitudes in Asia, *Bull. Seism. Soc. Am.*, 101, pp. 2201-2211, doi: 10.1785/0120100314.
- Yang, X., T. Lay, X. Xie, and M.S. Thorne, 2007, Geometric spreading of *Pn* and *Sn* in a spherical Earth model, *Bull. Seism. Soc. Am.*, 97, pp. 2053-2065.
- Zhao, L.F., X.B. Xie, W.M. Wang, and Z.X. Yao, 2008, Regional seismic characteristics of the October 9, 2006 North Korean nuclear test, *Bull. Seism. Soc. Am.*, 98, pp. 2571-2589, doi: 10.1785/0120080128.

DISTRIBUTION LIST

DTIC/OCP

8725 John J. Kingman Rd, Suite 0944

Ft Belvoir, VA 22060-6218

1 cy

AFRL/RVIL

Kirtland AFB, NM 87117-5776

2 cys

Official Record Copy

AFRL/RVBYE/Dr. Robert Raistrick

1 cy

This page is intentionally left blank.